

Review

# Metal Fluorides as Lithium-Ion Battery Materials: An Atomic Layer Deposition Perspective

Miia Mäntymäki <sup>1,2,\*</sup> , Mikko Ritala <sup>2</sup> and Markku Leskelä <sup>2</sup> 

<sup>1</sup> Picosun Oy, Tietotie 3, FI-02150 Espoo, Finland

<sup>2</sup> Department of Chemistry, P.O. Box 55 (A. I. Virtasen aukio 1), University of Helsinki, FI-00014 Helsinki, Finland; mikko.ritala@helsinki.fi (M.R.); markku.leskela@helsinki.fi (M.L.)

\* Correspondence: miia.mantymaki@picosun.com; Tel.: +358-50-320-6435

Received: 9 June 2018; Accepted: 6 August 2018; Published: 8 August 2018



**Abstract:** Lithium-ion batteries are the enabling technology for a variety of modern day devices, including cell phones, laptops and electric vehicles. To answer the energy and voltage demands of future applications, further materials engineering of the battery components is necessary. To that end, metal fluorides could provide interesting new conversion cathode and solid electrolyte materials for future batteries. To be applicable in thin film batteries, metal fluorides should be deposited with a method providing a high level of control over uniformity and conformality on various substrate materials and geometries. Atomic layer deposition (ALD), a method widely used in microelectronics, offers unrivalled film uniformity and conformality, in conjunction with strict control of film composition. In this review, the basics of lithium-ion batteries are shortly introduced, followed by a discussion of metal fluorides as potential lithium-ion battery materials. The basics of ALD are then covered, followed by a review of some conventional lithium-ion battery materials that have been deposited by ALD. Finally, metal fluoride ALD processes reported in the literature are comprehensively reviewed. It is clear that more research on the ALD of fluorides is needed, especially transition metal fluorides, to expand the number of potential battery materials available.

**Keywords:** atomic layer deposition (ALD); lithium-ion batteries; fluoride; thin films

## 1. Introduction

The technological advancements that have taken place during the last few decades have created the need to store more energy in ever smaller volumes. Lithium-ion batteries can store large amounts of energy in small weights and volumes, making them the technology-of-choice for multiple applications. In addition to their use in everyday portable electronics and all-electric vehicles, lithium-ion batteries could also provide a way to store large amounts of energy harnessed by using solar cells and wind turbines [1]. It is clear that the market for lithium-ion batteries will continue to increase in the years to come [2,3]. However, urgent materials engineering advances are needed to enable the continued progress of the technology and answer the high demands of future applications.

The most widely used lithium-ion battery materials include oxides and phosphates for cathodes [4,5]. These materials are intercalation electrodes and thus have relatively low usable capacities of 100–150 mAh/g. Graphitic carbon is the most frequently used anode material, with spinel lithium titanate and elemental silicon gaining more interest: the titanate for its enhanced safety and elemental silicon for its huge maximum capacity of 3600 mAh/g, made possible by its alloying reaction with lithium [4,5]. Alloying anodes have presented challenges in battery fabrication, because large volume changes associated with the alloying reactions can lead to electrode pulverization and degradation. However, with recent advances in nanofabrication, these problems might soon be mitigated by the use of proper micro- and nanoscale battery constructions [6–10].

Whereas high capacity alternatives, such as silicon, are already being intensely studied to replace the present anode materials, oxide and phosphate materials still dominate the research on cathodes, despite their limited capacities. Fluorides were studied extensively in the 1960s and 1970s for use in primary lithium batteries (i.e., batteries that would not be rechargeable) due to their high theoretical capacities and energy densities [11]. It was hoped that these materials would act as conversion cathodes, forming lithium fluoride during discharge (Equation (1)):



Conversion cathodes generally suffer from the same volume change problems as alloying anodes. However, by using the same nanofabrication methods as for anodes, these materials could provide a new, interesting class of lithium-ion battery electrode materials. Additionally, fluorides have also been reported to show high lithium-ion conductivities, making them possible solid electrolytes for all-solid-state thin film batteries [12–14].

Many enhancements in lithium-ion battery properties can be achieved by depositing component thin films onto 3D substrate geometries, as both active materials and protective layers on the active materials. During the 21st century, the thin film manufacturing method known as atomic layer deposition (ALD) has become a vital enabler of progressive technology nodes in microelectronics and is now becoming similarly important in the fabrication of Li-ion batteries. The advantages of ALD, including high film uniformity and excellent conformality over high-aspect-ratio substrates, make it ideal for the deposition of materials for ever-smaller, more complicated batteries: strict conformality is especially important for integrated, all-solid-state batteries, in which the small electrode thin film thicknesses can still produce high energy densities per footprint area when deposited into deep trenches [8]. The deposition of solid electrolyte materials, instead of using the current liquid electrolytes, could solve many of the safety issues associated with lithium-ion batteries.

This review briefly introduces the basic concept of lithium-ion batteries, some of the materials currently used in these batteries and the use of ALD in depositing these materials. Liquid electrolytes will not be discussed but instead potential inorganic solid electrolytes are shortly reviewed. Fluoride materials are presented as a potential “new” class of battery materials with uses as both electrodes and solid electrolytes for lithium-ion batteries. To motivate further studies on fluoride deposition using ALD, the literature in this area is reviewed.

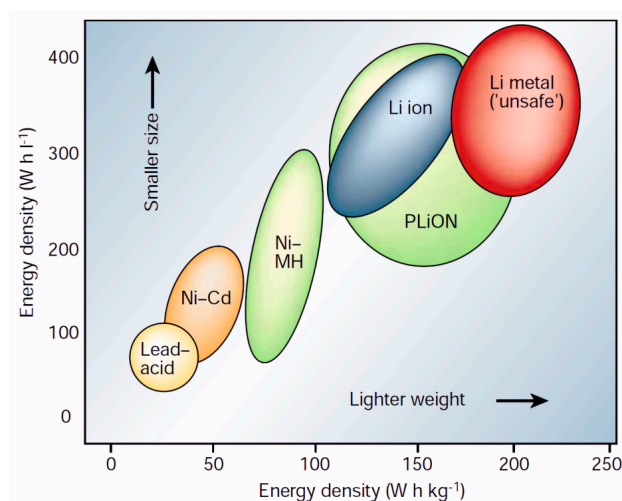
## 2. The Lithium-Ion Battery

### 2.1. Basic Principle

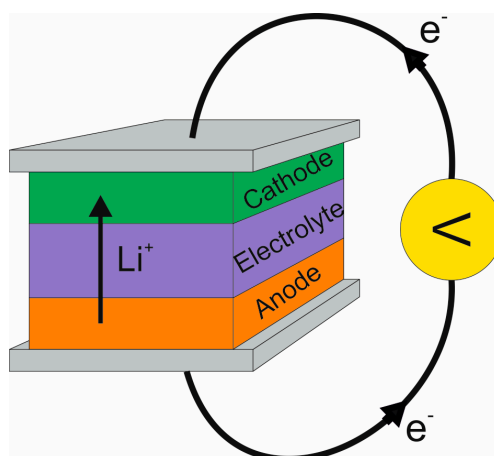
Lithium-ion batteries are used for energy storage in applications ranging from cell phones and laptops to electric vehicles. The basic concept of a lithium-ion battery is the same as for any other battery: chemical energy stored in the electrodes is converted into electrical energy via a chemical reaction. Some of the battery types in use today are depicted in Figure 1. As can be seen, lithium-ion batteries have surpassed many of the older battery technologies in energy density. This is related to the fact that lithium ions are relatively small and light-weight, which makes it possible to obtain high energy densities from lithium-containing materials. In addition, lithium forms compounds with large enough potentials to produce so-called “high quality” energy, or high power densities [15]. The small size of the lithium-ion is also an advantage in that lithium-ions are highly mobile in many materials, ensuring only low energy losses due to kinetic effects.

Figure 2 depicts the basic schematic of a lithium-ion battery. The battery consists of two electrodes (the positive cathode and the negative anode), an electrolyte and two current collectors. Because the active materials in the battery, the electrodes, are separated by an inert electrolyte, the energy liberated in the chemical reaction between the electrode materials can be converted into electrical work. During battery operation, lithium-ions flow through the electrolyte from the anode to the cathode.

At the same time electrons flow in the outer circuit from the anode to the cathode, balancing the net charge flow. These electrons can be used to do work, such as operate a laptop.



**Figure 1.** Comparison of energy densities in different battery types in use today. Reprinted with permission from [16]. Copyright 2001 Springer Nature.



**Figure 2.** Basic schematic of a lithium-ion battery, showing the flow of lithium ions and electrons during discharge.

In addition to the high energy and power densities, interest in lithium-ion batteries derives from the fact that most of them can be recharged multiple times without prohibitive loss of battery capacity. During recharging a voltage is applied to the outer circuit, which reverses the flow of electrons and  $\text{Li}^+$ -ions, moving them from the cathode to the anode. During the charge-discharge cycling, the battery capacity should stay as constant as possible. Usually the capacity slowly degrades with increased cycling as a result of, for example, reactions between the electrolyte and the electrodes and changes in the morphology of the electrodes, such as breakage or delamination [15].

Most lithium-ion batteries employ an organic liquid electrolyte material, composed of organic carbonates such as ethylene, dimethyl and diethyl carbonates, lithium hexafluorophosphate and potentially different additives [5,15]. Liquid electrolytes enable very high lithium-ion conductivities, which are beneficial for the battery operation. At the same time, the electrolyte should be an electron insulator so that no self-discharge takes place [15]. Liquid electrolytes can accommodate volume changes in the electrodes during cycling, which reduces stress in the battery. However, liquid electrolytes are also a major reason for the safety concerns of lithium-ion batteries: the electrolyte can

decompose at the electrodes, most often on the anode and form a solid-electrolyte interphase layer, or SEI-layer [15]. Commonly the SEI-layer protects the electrodes from further reactions with the electrolyte but in the event of an incomplete SEI-formation, reactions can proceed further with pressure building up inside the battery. Since the electrolyte materials are flammable, explosions can occur [17].

## 2.2. Conventional Electrode Materials

The electrodes define the capacity and voltage of any battery. Since both lithium-ions and electrons move inside the electrodes, the materials need to be both ion and electron conductors. The reactions taking place in the electrodes can be roughly divided into conversion reactions, alloying reactions and insertion or intercalation reactions (Figure 3) [4]. Conversion and alloying electrodes generally provide higher battery capacities but there can be problems with electrode degradation during cycling due to repeated volume changes associated with the conversion reaction. Thus, conversion and alloying electrodes have more often been used in primary batteries, meaning non-rechargeable batteries.

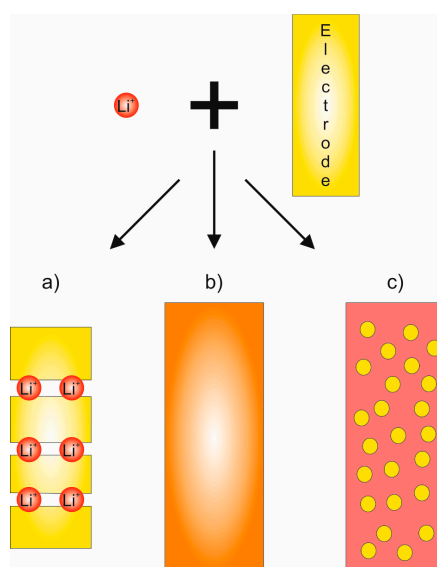


**Figure 3.** Schematic illustrating the different kinds of reactions possible with lithium ions and electrode materials. (a) Intercalation; (b) Alloying; (c) Conversion. With alloying and conversion reactions, significant volume changes often take place in the electrode.

In rechargeable, or secondary, batteries intercalation reactions are the most commonly used, with the  $\text{LiCoO}_2\text{-C}_6$  (graphite) battery being a prime example of this reaction. Even if intercalation electrodes do not generally suffer from volume changes of similar magnitude to conversion electrodes, they still require care in the charging-discharging process: too deep charge-discharge cycling can lead to irreversible changes in the electrode structure, which in turn can lead to a diminished battery capacity.

### 2.2.1. Cathodes

Intercalation cathode materials are most often lithium containing transition metal oxides, in which the insertion and extraction of lithium is made possible by the redox capabilities of the transition metal [4,18]. Although  $\text{LiCoO}_2$  is the most commonly used cathode material, manganese and nickel oxides are gaining interest as possible future cathodes [18,19]. Table 1 contains the potentials and capacities obtainable from some of the most studied cathode materials. Despite their common use in batteries today, transition metal oxide cathodes have some serious drawbacks. Firstly, the potentials obtainable from these materials are limited, which is a problem especially for high power density applications. Secondly, the capacities available from these materials are quite low as a result of the limited amount of lithium available before irreversible changes in the structures occur. For example,

only half of the lithium-ions in  $\text{LiCoO}_2$  can be reversibly utilized [19]. Lastly, liquid electrolytes are known to give rise to dissolution of the transition metal, thus decreasing the cathode capacity even further [18]. However, thin film methods such as atomic layer deposition can be used to deposit thin layers (e.g.,  $\text{Al}_2\text{O}_3$  or  $\text{AlF}_3$ ) onto cathode materials to protect them from side reactions such as transition metal dissolution [20–24]. Some of these problems can also be circumvented by using mixture cathodes, such as  $\text{LiNi}_{(1-y-z)}\text{Mn}_y\text{Co}_z\text{O}_2$ , which can also produce slightly higher capacities [5,18,19]. In addition to oxides, sulphates and phosphates, such as  $\text{LiFePO}_4$ , have also been studied extensively [19]. Despite being cheaper and less toxic than most cathode materials and providing a reasonable capacity,  $\text{LiFePO}_4$  suffers from low electronic conductivity, limiting its applicability [19]. For cathodes, alloying and conversion reactions have not gained much attention.

**Table 1.** Potentials and capacities obtainable from some of the most studied lithium-ion battery cathode materials.

Material	Type	Potential (V) (vs. $\text{Li}/\text{Li}^+$ )	Specific Capacity (mAh/g)	Ref.
$\text{LiCoO}_2$	Intercalation	~3.9	140	[4]
$\text{LiNiO}_2$	Intercalation	2.7–4.1	140–200	[4,19]
$\text{LiMn}_2\text{O}_4$	Intercalation	3.5–4.5	150	[4]
$\text{LiFePO}_4$	Intercalation	3.4	170	[4,5,19]
$\text{V}_2\text{O}_5$	Intercalation	3.2–3.4	120	[4]

### 2.2.2. Anodes

Table 2 presents some potential anode materials for lithium-ion batteries. For an anode, a potential as low as possible is desired to reach a high cell voltage. As with the cathode materials, intercalation anodes are more common than the other types of anodes. However, a lot of work is now being put into studying materials such as silicon and tin as lithium-ion battery alloying anodes [4,5,9,25].

**Table 2.** Potentials and capacities obtainable from some of the most studied lithium-ion battery anode materials.

Material	Type	Potential (V) (vs. $\text{Li}^+/\text{Li}$ )	Specific Capacity (mAh/g)	Ref.
$\text{C}_6$	Intercalation	<0.6	370	[4,5]
$\text{Li}_4\text{Ti}_5\text{O}_{12}$	Intercalation	1.5	175	[4]
Li	Alloying	0	3800	[26]
Si	Alloying	0.1–0.3	3580	[4,5]
Sn	Alloying	0.6–0.8	990	[4,5,9]
MO (M = $\text{Co}^{2+}$ , $\text{Fe}^{2+}$ , $\text{Cu}^{2+}$ , $\text{Ni}^{2+}$ )	Conversion	~1.8–2.0	670–750	[27–29]

Metallic lithium was, unsurprisingly, the first choice for the anode of a lithium-ion battery [18,26]. However, safety concerns such as dendrite formation [26] have moved the interest towards other anodes such as graphitic carbon  $\text{C}_6$ , which produces capacities of 370 mAh/g [5,15]. The use of  $\text{C}_6$  still does not help avoid dendritic lithium deposition due to the very low electrode potential of carbon anodes. One possible replacement for carbon is the spinel lithium titanate  $\text{Li}_4\text{Ti}_5\text{O}_{12}$ , which has a reasonable capacity with a very small volume expansion during lithiation. In addition, the titanate is environmentally benign with a reasonable cost [28]. A major drawback of this material and many insertion oxide anodes in general, is the high electrode potential, which results in cells with low operation voltages [5,28].

Of the alloying anodes, elemental silicon has attracted much attention because of its low cost, abundance in nature and high specific capacity of over 3500 mAh/g [28]. However, alloying the maximum 3.75 lithium-ions per one Si atom produces volume changes of up to 300% in the electrode, limiting the cycling ability of the anode [5]. Nanostructured silicon is now studied in the hope of

alleviating the problems with volume expansion [5,9]. In addition, atomic layer deposition has been utilized in contact with Si anodes to improve their mechanical integrity and to stabilize the interfaces of the anode [10].

Similarly, elemental tin has attracted much attention but suffers from the same problems as silicon [9]. Attempts have been made to circumvent the volume change problems by using conversion anodes composed of, for example SnO or SnO<sub>2</sub>. In these anodes, lithium first forms lithium oxide and tin is reduced to metallic tin, which can further alloy lithium and is responsible for the reversible capacity [28]. However, the problems related to volume changes still persist to some extent in these anodes [28]. Many transition metal oxides have also been studied as conversion anodes, with capacities ranging from 600 to 700 mAh/g [27]. In addition to the persisting volume change problem, conversion anodes often also suffer from large overpotentials [9].

### 2.3. Conventional Solid Electrolyte Materials

Solid electrolyte materials are the enablers of all-solid-state Li-ion batteries. These materials have stringent property demands: they must be unreactive at the electrode potentials and have a high lithium-ion conductivity at room temperature [15,30]. In addition, they must be good electron insulators to avoid self-discharge and short-circuits [4]. Despite the high specification for material properties, a vast number of solid electrolyte materials suitable for lithium-ion batteries have been reported in the literature [30–33]. In addition to inorganic ceramics, composites and polymer mixtures can be used as solid electrolytes [31,33,34].

Inorganic fast lithium-ion conducting materials can be single-crystalline, polycrystalline or amorphous, with many different structural types reported for the crystalline materials (Table 3, Figure 4) [31,32]. Generally, an amorphous electrolyte material would be preferred as grain boundaries in crystalline materials can lead to both impeded ion movement and electron leakage and thus poorer insulating properties [33,34]. In addition, amorphous materials can provide isotropic lithium-ion conduction in a wide range of different compositions [32].

**Table 3.** Structures and ionic conductivities of some of the most studied solid inorganic lithium-ion conducting materials.

Material	Structure	Ionic Conductivity at RT (S/cm)	Ref.
LiPON	Amorphous	$10^{-8}$ – $10^{-6}$	[31,32]
Li <sub>2</sub> O–SiO <sub>2</sub> –V <sub>2</sub> O <sub>5</sub> (LVSO)	Crystalline/Amorphous	$10^{-7}$ – $10^{-5}$	[32]
Li <sub>2</sub> S–GeS <sub>2</sub> –Ga <sub>2</sub> S <sub>3</sub>	Amorphous	$10^{-4}$	[32]
(Li,La)TiO <sub>3</sub> (LLT)	Perovskite	$10^{-3}$	[31,33]
LiTi <sub>2</sub> (PO <sub>4</sub> ) <sub>3</sub>	NASICON	$10^{-5}$	[31,32]
Li <sub>14</sub> ZnGe <sub>4</sub> O <sub>16</sub>	LISICON	$10^{-6}$	[33]
Li <sub>6</sub> BaLa <sub>2</sub> Ta <sub>2</sub> O <sub>12</sub>	Garnet	$10^{-5}$	[31]

Amorphous, or glassy, electrolytes can be roughly divided into oxide and sulphide glasses [32]. Probably the most studied amorphous solid electrolyte material is nitrogen doped lithium phosphate (lithium phosphorus oxynitride), LiPON, which is in fact already in use in thin film lithium-ion batteries [32,33]. The material is usually deposited by sputtering in a nitrogen atmosphere and the resulting films have lithium-ion conductivities of the order of  $10^{-8}$ – $10^{-6}$  S/cm [32], as compared to the  $\sim 10^{-2}$  S/cm for liquid electrolytes [5]. The success of LiPON comes not only from its reasonably high lithium-ion conductivity but also from its excellent stability against the electrode materials [32]. Sulphide glasses, on the other hand, have been studied much less than the corresponding oxides, mostly because of their reactivity in air and corrosiveness [32].

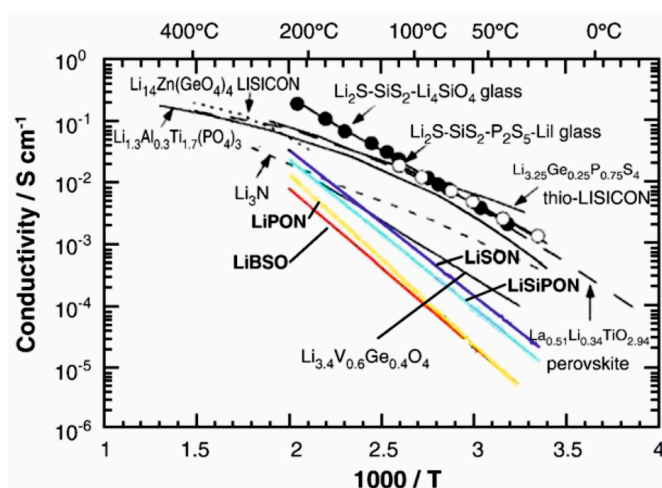


**Figure 4.** Bulk ionic conductivities of selected oxides and phosphates as a function of temperature. Reprinted with permission from [33]. Copyright 2009 Elsevier.

Out of crystalline electrolyte materials, the perovskite  $(\text{Li},\text{La})\text{TiO}_3$  (LLT) is known to show high bulk conductivity. However, reduction of  $\text{Ti}^{4+}$  and the consequent increase in electronic conduction are problems associated with this material [31,33]. Titanium-free perovskites, such as  $(\text{Li},\text{La})\text{NbO}_3$  have thus been studied [32]. Phosphates with the NASICON (sodium superionic conductor) structure are also known to show high lithium-ion conductivities [32]. In Table 3  $\text{LiTi}_2(\text{PO}_4)_3$  is given as an example but many other +IV oxidation state metals can be substituted for titanium in the structure. LISICON (lithium superionic conductor) materials, on the other hand, are mixtures of lithium silicates or germanates, lithium phosphates or vanadates and lithium sulphates and can produce similar conductivities as the NASICON structures [32]. In addition to these material classes, oxides such as  $\text{Li}_6\text{BaLa}_2\text{Ta}_2\text{O}_{12}$  with the garnet structure have been studied extensively and shown to have reasonable ionic conductivities [31]. Another benefit of the garnet materials is their high chemical stability in contact with the electrodes [32].

### 3. Metal Fluorides as Lithium-Ion Battery Materials

Metal fluorides can be utilized in lithium-ion batteries in many ways [11]. This review will focus only on metal fluorides as electrodes, artificial SEI-layers and solid electrolytes. The reader is advised that much work has also been done on other fluorinated materials in batteries, such as fluorinated salts as additives in liquid electrolytes [11,35], fluorinated solvents in batteries [35], carbon fluorides as negative electrodes [11] and fluorinated binder materials [11,35]. These topics will not be discussed further here.

#### 3.1. Electrode Materials

Amatucci and Pereira note in their review on metal fluoride based electrode materials that “The use of fluorides stems from the intrinsic stability of fluorinated materials and their ability to generate high electrochemical energy as electrodes” [11]. Indeed, metal fluoride cathodes generally produce higher potentials than the corresponding oxides of the same redox-couple, which can lead to higher energy densities [11]. Thus, fluoride materials could be used in high voltage batteries, where the stability of active materials is especially important. Fluorides can be used as cathodes either as pure fluorides or as doped materials, such as oxyfluorides, fluorosulphates or fluorophosphates [11,35]. Fluoride doping has been reported to improve capacity retention of intercalation cathodes such as lithium nickel oxide and lithium nickel cobalt oxide [11]. This could be related to a slower dissolution of transition metals into liquid electrolytes from the oxyfluorides [11]. For fluorophosphate cathodes, such as  $\text{Li}_2\text{CoPO}_4\text{F}$ , high potentials of over 5 V are obtainable, accompanied again by a slower dissolution of the transition

metal [11,35]. However, the performance of these cathodes is limited due to poor ionic and electronic conductivity and instability of liquid electrolytes at such high potentials [35].

As already mentioned in the Introduction, pure metal fluorides gained interest decades ago as electrodes for primary batteries because of their high capacities (Figure 5). With the increased interest in high capacity alloying and conversion anodes such as Si and SnO<sub>2</sub>, fluoride conversion cathodes could also resurface as interesting materials for secondary lithium-ion batteries [11,25,29,36–39]. Similar to alloying anodes, fluoride conversion cathodes suffer from large volume changes and subsequent pulverization during cycling. In addition, fluorides are very poor electron conductors due to their high band gaps and often show high overpotentials, which can make their integration as reversible electrodes challenging [25,29]. In the early years materials such as CuF<sub>2</sub> and HgF<sub>2</sub> were studied but with little success. Recently, interesting progress has been made in this research area. For example, BiF<sub>3</sub>, FeF<sub>2</sub> and FeF<sub>3</sub> have been studied extensively as cathodes using nanocomposites of the metal fluorides and conductive carbon [38,40]. Using nanocomposites with carbon can not only help with the volume change but also with the inherently low electrical conductivity of fluoride materials.

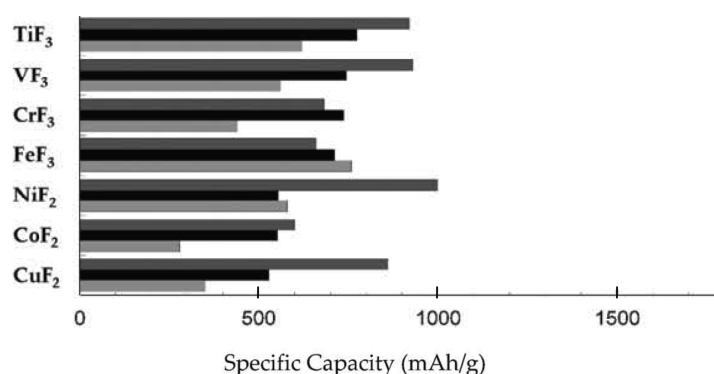


**Figure 5.** Theoretical (black), first discharge (dark grey) and charge (light grey) specific capacities of conversion fluoride cathode materials. Adapted with permission from [36]. Copyright 2010 Wiley-VCH.

Due to the work on primary batteries pure fluorides are generally considered only as conversion cathodes but some reports on intercalation fluorides have been published [41–43]. For example, Li<sub>3</sub>FeF<sub>6</sub> has been reported to show intercalation of 0.7–1 Li<sup>+</sup> ions per fluoride unit in a carbon nanocomposite form, resulting in a reversible capacity of 100–140 mAh/g [41,42]. The capacity depends on the size of the Li<sub>3</sub>FeF<sub>6</sub> particles, with smaller particles resulting in a higher capacity [42]. A deeper discharge of the material was reported to lead to LiF formation, indicating a conversion reaction at low potentials. Similarly, a nanocomposite of Li<sub>3</sub>VF<sub>6</sub> was reported to reversibly intercalate up to one Li<sup>+</sup> per fluoride unit [43]. Calculations predict that fluorides such as LiCaCoF<sub>6</sub> could provide very high intercalation voltages [44].

In addition to their potential use as electrode materials, fluorides can also be utilized as solid-electrolyte-interface layers deposited on the more conventional electrode materials to protect them from reactions with the organic liquid electrolytes. AlF<sub>3</sub> has been studied extensively in this regard, on both cathodes [45–49] and anodes [50]. AlF<sub>3</sub> is suitable for electrode protection because it is rather inert and the Al<sup>3+</sup>-ion cannot be reduced or oxidized in battery conditions [20]. The material has been reported to decrease the irreversible capacity losses of electrodes and improve cycling stability, [45,47] and increase the thermal stability of electrodes [45,46,49]. Figure 6 illustrates how a layer of AlF<sub>3</sub> can increase the capacity retention in a lithium cobalt nickel manganese oxide cathode. Using too much AlF<sub>3</sub>, however, decreases the capacity considerably.

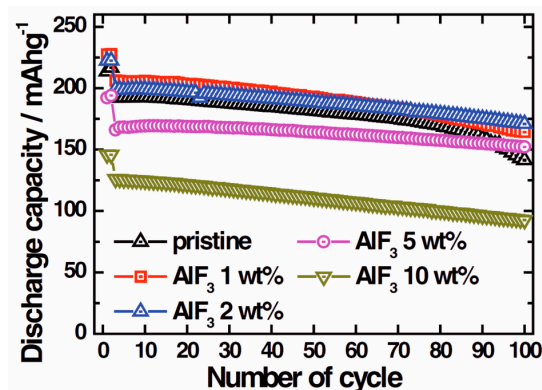


**Figure 6.** The effect of an  $\text{AlF}_3$  coating on the discharge capacity of a lithium cobalt nickel manganese oxide cathode as a function of the number of charge/discharge cycles. Reprinted with permission from [47]. Copyright 2012 Wiley-VCH.

### 3.2. Solid Electrolyte Materials

The applicability of metal fluorides as solid electrolytes for  $\text{Li}^+$  ions has not been studied as extensively as their use as electrodes. However, some examples of potential electrolyte materials can be found in the literature.  $\text{Li}_3\text{AlF}_6$ , a stoichiometric ternary of  $\text{LiF}$  and  $\text{AlF}_3$ , has been reported to show high ionic conductivities of the order of  $10^{-6}$  S/cm in thin film form [12–14,51]. In addition, milling this ternary fluoride with  $\text{LiCl}$  has been reported to lead to high conductivities [52]. Other fluorides that also show high conductivities when mixed with  $\text{LiF}$  include  $\text{NiF}_2$ ,  $\text{VF}_3$ ,  $\text{CrF}_3$  and  $\text{YF}_3$  (Figure 7) [13,53]. These materials have been deposited by thermal evaporation and fast quenching, resulting in amorphous thin films. The increased ionic conductivity in these mixtures is attributed to the formation of amorphous intermediate phases with high coordination numbers for lithium, such as in the  $\text{Li}_3\text{AlF}_6$  phase [13]. Even more complicated fluoride mixtures have been studied as well [12,14,54–56], such as the  $\text{LiF}-\text{AlF}_3-\text{ScF}_3$  system, which can reach similar conductivity values as the pure  $\text{Li}_3\text{AlF}_6$  [12]. With fluoride glasses of the type  $\text{LiF}-\text{ZrF}_4-\text{LaF}_3$  high lithium-ion conductivities can be obtained for materials with sufficient  $\text{LiF}$  component [54].

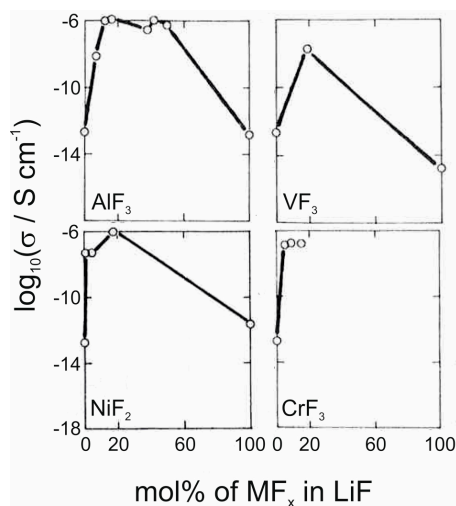


**Figure 7.** Room temperature ionic conductivities  $\log_{10}\sigma$  of fluoride thin films composed of  $\text{LiF}$  and  $\text{AlF}_3$ ,  $\text{VF}_3$ ,  $\text{NiF}_2$  or  $\text{CrF}_3$ . Adapted with permission from [13]. Copyright 1984 Elsevier.

In addition to the applications in lithium-ion batteries, some metal fluoride mixtures can act as electrolytes for  $\text{F}^-$ -ions, making high voltage fluoride-ion batteries a possibility [57–61]. Mixed fluoride

glasses can, in some cases, conduct both lithium- and fluoride-ions, depending on the molar ratios of the metal fluorides [54,56].

## 4. Atomic Layer Deposition

### 4.1. Basic Principle

Atomic layer deposition (ALD) is a gas phase thin film deposition method, best known for producing thin films of high uniformity and conformality. It is closely related to chemical vapour deposition (CVD). Whereas in CVD gaseous precursors are supplied simultaneously, in ALD precursor pulses are separated by purge gas pulses or evacuation periods, resulting in no gas phase reactions. Instead, the precursors react one at a time with the substrate or film surface groups in a digital manner [62,63]. ALD has different variations, including thermal ALD [64], plasma-enhanced ALD (PEALD) [65] and photo-ALD [66,67], depending on how energy is supplied to the deposition reaction. Thermal ALD refers to a process where the energy for the surface reactions is produced by heating. In PEALD, additional energy from radicals and, depending on the reactor configuration, possibly also ions and electrons, is used [65]. In photo-ALD reactions are enhanced with UV-and/or visible light [67].

The atomic layer deposition cycle is composed of four steps (Figure 8). In step 1, the first precursor adsorbs and reacts on a substrate surface. After all potential surface sites have reacted with the first precursor, excess precursor molecules and side products are purged or pumped away in step 2. In step 3, the second precursor reacts with the surface, forming a binary film. In step 4 reaction by-products and excess precursor two are purged and pumped away. By repeating the four-step cycle, a film of desired thickness can be formed [62]. Generally, a film of one monolayer or less is formed in one ALD cycle [68]. The amount of material deposited depends both on the density of active surface groups and the size of the precursor molecules [62,68].

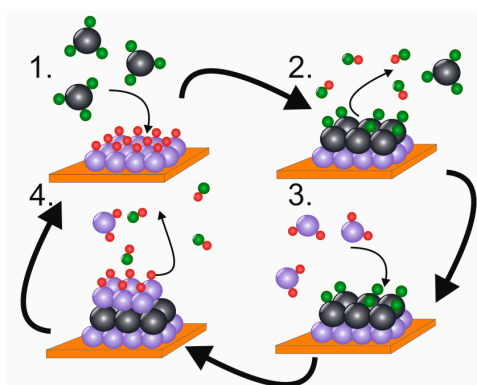


**Figure 8.** Schematic illustrating one cycle in ALD. 1. Precursor 1 molecules react with a surface covered with active sites; 2. Reaction side products and excess precursor are purged away; 3. Precursor 2 is introduced and it reacts with the surface covered with precursor 1 molecules; 4. The reaction side products and excess of precursor 2 are again purged away, resulting ideally in one monolayer of material on the substrate.

In ALD literature, the reaction type illustrated in Figure 8 has been traditionally called “ligand exchange” [68]: for example, in the case of  $\text{Al}_2\text{O}_3$  deposition trimethylaluminum (TMA) and water react in a way that methane is produced as a side product. Thus, it can be viewed as methyl ligands changing their bonding from aluminum in TMA to hydrogen from hydroxide surface groups. In synthesis work, this type of reaction is commonly called metathesis. This broad definition of ligand exchange can be applied to most ALD reactions in use today. Other ALD-type reactions include combustion with ozone and oxygen radicals, an additive reaction with elemental precursors and controlled decomposition of

an adsorbed species [64]. Ideal ALD processes should show an ALD window, meaning a temperature region where the film growth rate stays constant as a function of deposition temperature. However, usually small deviations from this behaviour are seen, because the number of active surface sites can be highly dependent on the deposition temperature [64]. As most often less than a monolayer is deposited per one ALD cycle, the slowness of the deposition process is considered as one of the greatest weaknesses of ALD [62].

All reactions in ALD occur between surface groups and adsorbing gaseous precursors, so the reactions become terminated when all the surface groups have reacted or when the steric hindrance from large precursor molecules prevents further precursor adsorption [68]. This results in self-limiting growth which means that using higher precursor doses, often in practice meaning longer precursor pulse times, will not result in more growth and that a constant amount of film is deposited in each cycle [62,64]. To achieve this self-limiting or saturative behaviour, it is important that the precursor does not self-decompose. In addition, long enough purge times between precursor pulses are required to ensure that no excess precursor remains in the gas phase or adsorbed onto the surface when the second precursor is introduced. Self-limiting growth enables the large area uniformity, excellent conformality and nanometre-level thickness control of ALD films: the growth per cycle is constant, which means that the film thickness can be specified by choosing a proper cycle number. Thus, with ALD even very demanding 3D structures can be covered with a film of constant thickness, when long enough precursor pulse times and purges are employed [62].

ALD is a promising method for the deposition of small, integrated 3D all-solid-state batteries due to the precision it affords in thickness control and conformality. All-solid-state batteries can be integrated into, for example, microelectromechanical systems (MEMS) to achieve autonomous sensing devices. For this type of integration, very small batteries are generally required because the size of the battery can limit the size of the whole device [8,17]. Making a battery smaller by using thinner active layers is a viable solution for all-solid-state batteries because thinner layers result in smaller transport losses and over-potentials due to smaller diffusion length scales [8,17,69]. Importantly, the limitations imposed by the low lithium-ion conductivities of solid electrolytes can thereby be circumvented [8]. However, thin electrode layers limit the energy available from the battery. By making batteries smaller with complex 3D structures, gains in both energy and power density can be achieved due to simple geometrical reasons: more active material can be packed into a smaller foot print area, with the advantages of short diffusion lengths still present [8].

#### *4.2. Atomic Layer Deposition of Conventional Lithium-Ion Battery Materials*

In this section, a few examples of the more conventional lithium-ion battery materials deposited by ALD are introduced. Examples of binary oxide electrodes (specifically  $V_2O_5$  and  $TiO_2$ ) and lithium containing materials are presented. Lithium containing materials are quite a new addition to the ALD materials toolbox—the first paper on the subject was published in 2009 [70]. Since then, this area of research has expanded very rapidly. Due to the mobility and reactivity of  $Li^+$  ions, ALD of lithium containing materials has additional process development issues in comparison to most other ALD processes and some of these issues are discussed in the following subsections. In this section emphasis is given to potential solid electrolyte materials, as these are generally considered the most difficult materials to deposit. For a more thorough review of this subject, both review articles and books are available [71–79]. In recent years, ALD has also been studied extensively as a method to modify the interfaces between the electrodes and the electrolyte by forming an artificial SEI-layer [75,80,81]. ALD  $Al_2O_3$  is generally used for this application and it has been found that a few ALD cycles can improve the cycling capability and capacity retention of the electrodes [80,81]. These results will not be discussed further here but the reader is advised that a lot of literature on this subject is available [80–83]. Some examples of ALD-made metal fluorides as artificial SEI layers will be shortly mentioned in Section 5.

## 4.2.1. Cathodes

Table 4 includes examples of some of the conventional lithium-ion battery cathode materials deposited by ALD. Both binary and ternary oxides and phosphates have been deposited for conventional batteries.  $\text{Li}_2\text{S}$  has been envisioned as a cathode for lithium-sulphur batteries [84].

**Table 4.** Examples of conventional lithium-ion battery cathode materials deposited by ALD. Abbreviations used:  $\text{O}^i\text{Pr}$  = *iso*-propoxide,  $\text{O}^t\text{Bu}$  = *tert*-butoxide, Cp = cyclopentadienyl, TMPO = trimethyl phosphate, thd = 2,2,6,6-tetramethyl-3,5-heptanedionato.

Material	Precursors	$T_{\text{Dep}}$ (°C)	Growth Rate (Å)/Binary Cycle	Capacity (mAh/g)	Ref.
$\text{V}_2\text{O}_5$	$\text{VO}(\text{O}^i\text{Pr})_3 + \text{H}_2\text{O}$	105	0.15–0.2	455	[85,86]
$\text{V}_2\text{O}_5$	$\text{VO}(\text{O}^i\text{Pr})_3 + \text{O}_3$	170–185	0.25	440	[86]
$\text{Li}_x\text{Co}_y\text{O}$	$\text{LiO}^t\text{Bu} + \text{CoCp}_2 + \text{O}_2$ plasma	325	1.0 with Li:Co pulsing ratio 1:1	96 for Li:Co pulsing 1:4	[87,88]
$\text{Li}_x\text{Fe}_y\text{PO}_4$	$\text{LiO}^t\text{Bu} + \text{FeCp}_2 + \text{O}_3 +$ TMPO + $\text{H}_2\text{O}$	300	0.85 with Li:Fe pulsing ratio 1:5	150 at 0.1 C	[89]
$\text{Li}_x\text{Mn}_y\text{O}$	Lithd + $\text{Mn}(\text{thd})_3 + \text{O}_3$	225	0.2 with Li:Mn pulsing ratio 1:19	–	[90]
$\text{Li}_x\text{Mn}_y\text{O}$	$\text{LiO}^t\text{Bu} + \text{H}_2\text{O}$ or Lithd + $\text{O}_3$ on $\text{MnO}_2$	225	–	230	[90]
$\text{Li}_2\text{S}$	$\text{LiO}^t\text{Bu} + \text{H}_2\text{S}$	150–300	1.1 at 150–300 °C	500	[91]

Vanadium oxide was one of the earliest materials to be deposited by ALD for lithium-ion batteries [85,86,92]. Vanadyl tris-*iso*-propoxide with either water or ozone as co-reactant have been used as precursors for this material. Using water produces amorphous films, while with ozone crystalline films can be obtained. Crystalline and amorphous films produce different capacities depending on the extent of lithium intercalation, with crystalline films having higher capacities when 1 or 2 Li-ions intercalate per one  $\text{V}_2\text{O}_5$  unit [86]. A surprisingly high capacity of 455 mAh/g has been reported for 200 nm of amorphous  $\text{V}_2\text{O}_5$  between 1.5 and 4.0 V (Li/Li<sup>+</sup>) [85]. This high value is related to the large potential range used for cycling, resulting in 3 Li-ions intercalating per one  $\text{V}_2\text{O}_5$  [85]. For a thicker amorphous film of 450 nm, a capacity of 275 mAh/g was obtained in the same range. Both the thicker and the thinner films showed reasonable capacity retention after 90 cycles. For crystalline films, capacities of 127–142 mAh/g have been obtained in the potential range 2.6–4.0 V (1 Li per  $\text{V}_2\text{O}_5$ ) [86]. Between 1.5 and 4.0 V (3 Li per  $\text{V}_2\text{O}_5$ ), a capacity of 440 mAh/g is obtainable but the capacity degrades to 389 mAh/g already in the second cycle.

As already discussed, lithium cobalt oxide  $\text{LiCoO}_2$  is currently the most often used cathode material in lithium-ion batteries. Despite this, only two reports from one group on the deposition of  $\text{LiCoO}_2$  by ALD can be found in the literature [87,88]. It appears that the challenges in cobalt oxide deposition have had an effect on the research of the lithiated material. The reported  $\text{LiCoO}_2$  process makes use of oxygen plasma combined with  $\text{CoCp}_2$  (cobaltocene) and  $\text{LiO}^t\text{Bu}$  (lithium *tert*-butoxide). The deposition supercycle consists of  $\text{Co}_3\text{O}_4$  and  $\text{Li}_2\text{CO}_3$  subcycles and the effect of different pulsing ratios on film properties was studied. The process showed saturation with both metal precursors with Li:Co = 1:1 pulsing ratio and the film thickness increased fairly linearly with the number of cycles when using a 1:4 pulsing ratio. After annealing the films consisted of the hexagonal phase of  $\text{LiCoO}_2$  according to both Raman and GIXRD (grazing incidence X-ray diffraction) measurements. Electrochemical characterization revealed that a 12% capacity loss was evident between charge and discharge cycles. For a film deposited with a 1:4 pulsing ratio, the capacity was only about 60% of the theoretical value. For a 1:2 ratio film, the capacity was even lower, which might be explained by the higher impurity contents in this film. With the 1:4 pulsing ratio, the composition of the films was  $\text{Li}_{1.2}\text{CoO}_{3.5}$ , as determined by elastic backscattering [88].

The potential cathode material lithium iron phosphate,  $\text{LiFePO}_4$ , has also been the subject of ALD studies [89,93]. The material has been deposited at 300 °C on silicon substrates using

ferrocene and ozone as precursors for the  $\text{Fe}_2\text{O}_3$  subcycle, trimethylphosphate (TMPO) and water for  $\text{PO}_x$  and lithium *tert*-butoxide and water for the  $\text{Li}_2\text{O}/\text{LiOH}$  subcycle [89]. Iron oxide and the phosphate were pulsed sequentially for five cycles, after which one cycle of  $\text{Li}_2\text{O}/\text{LiOH}$  was applied. The resulting films were amorphous and showed a linear increase in thickness as a function of deposited supercycles. The material could also be deposited onto carbon nanotubes (CNTs) [87]. The CNT-based films were amorphous but crystallization to orthorhombic  $\text{LiFePO}_4$  was observed after annealing in argon at  $700\text{ }^\circ\text{C}$  for 5 h. The Fe:P ratio in the annealed film was 0.9, as determined by EDX (energy-dispersive X-ray spectroscopy). Unfortunately, no compositional information on Li content was given. The  $\text{LiFePO}_4$  film deposited onto CNTs showed good electrical performance, with clear redox peaks in a cyclic voltammetry curve at 3.5 V and 3.3 V (vs.  $\text{Li}/\text{Li}^+$ ) and a discharge capacity of 150 mAh/g at 0.1 C [89]. Encouragingly, the material could maintain a discharge capacity of 120 mAh/g at 1 C even after 2000 cycles.

$\text{LiFePO}_4$  has also been deposited using metal-thd complexes [93]. Pulsing Lithd (lithium 2,2,6,6-tetramethyl-3,5-heptanedionate) and ozone between subcycles of  $\text{Fe}(\text{thd})_3 + \text{O}_3$  and  $\text{TMPO} + \text{O}_3 + \text{H}_2\text{O}$  resulted in stoichiometric  $\text{LiFePO}_4$  when the fraction of  $\text{Li}_2\text{CO}_3$  subcycles was 37.5%. The as-deposited films were amorphous but could be crystallized in 10/90  $\text{H}_2/\text{Ar}$  atmosphere at  $500\text{ }^\circ\text{C}$ . These films were reported to show poor electrical conductivity, as expected with this material [19], however very little additional information was given. It should be noted that the same research group has also published an ALD process for the de-lithiated cathode material  $\text{FePO}_4$  [94]. They reported an initial electrochemical capacity of 159 mAh/g for the as-deposited, amorphous 46 nm thick  $\text{FePO}_4$  film. The capacity increased to 175 mAh/g after 230 charge-discharge cycles and after 600 cycles the capacity was still 165 mAh/g.

Lithium manganese spinel  $\text{Li}_x\text{Mn}_2\text{O}_4$  is an interesting cathode material for lithium-ion batteries due to its low volume change during (de)lithiation, high voltage and environmentally benign elements. The material has been deposited by ALD by Miikkulainen et al. using various methods [90]. Firstly,  $\text{Mn}(\text{thd})_3$  and ozone were used as precursors for manganese oxide and this process was combined with the  $\text{Lithd} + \text{O}_3$  process for lithium incorporation. Interestingly, even with exceedingly small numbers of  $\text{Li}_2\text{CO}_3$  subcycles, high  $\text{Li}^+$  incorporation was achieved, with only a 5%  $\text{Li}_2\text{CO}_3$  pulsing leading to a Li:Mn ratio of 1:1. This was in fact the maximum content of lithium obtained: using larger numbers of  $\text{Li}_2\text{CO}_3$  subcycles led to a decrease in uniformity. To achieve the stoichiometric lithium level for  $\text{LiMn}_2\text{O}_4$ , 1% of  $\text{Li}_2\text{CO}_3$  pulsing was sufficient. All the films showed the crystalline spinel phase as-deposited, with  $\text{MnO}_2$  impurities present in the films with the lowest lithium concentrations. Crystalline spinel  $\text{LiMn}_2\text{O}_4$  was also obtained by using  $\text{LiO}^t\text{Bu}$  and water as precursors, however little else was reported on this process.

The lithium manganese spinel process is unique in that while the growth rate of the films stays rather constant at below  $0.3\text{ \AA}/\text{cycle}$ , the lithium content increases very rapidly and reaches a high value with very small Li-subcycle numbers [90]. This indicates that the mechanism of this process differs significantly from conventional ternary ALD processes. Another clue about the mechanism was given by ToF-ERDA (time-of-flight elastic recoil detection analysis) elemental depth profiles which showed uniform film composition, albeit with a lithium deficiency on the film surface. To achieve such high lithium concentrations, either more than one monolayer should be deposited in one subcycle, or the growth should include a bulk component in addition to the normal surface reactions. Multilayer growth could be assumed to lead to lithium excess on the film surface, since lithium carbonate was always the last material deposited. Therefore, the bulk must be playing a role in the deposition process. Miikkulainen et al. postulated that the reduction needed for manganese to change from +IV in  $\text{MnO}_2$  to +III/+IV in  $\text{LiMn}_2\text{O}_4$  takes place during the  $\text{Lithd}$  pulse, which affects not only the surface but also deeper parts of the film [90]. The following ozone pulse removes organic residues from the surface and re-oxidizes the topmost manganese ions on the surface. This reaction then drives lithium ions deeper into the film, resulting in a uniform elemental distribution with a slightly lithium deficient surface.

Miikkulainen et al. continued their studies on  $\text{LiMn}_2\text{O}_4$ , using both  $\text{LiO}^t\text{Bu}$  and water and Lithd and ozone exposures on  $\text{MnO}_2$  at 225 °C [90]. Interestingly, 110 nm of manganese oxide could be converted to the spinel phase with only 100 cycles of the lithium carbonate process applied on top of the film. The carbonate was not present in the X-ray diffractogram. Lithiation was achieved to some extent also without ozone pulses. The manganese oxide films lithiated with  $\text{LiO}^t\text{Bu}$  and water in a similar manner showed the best electrochemical storage properties, with a capacity of 230 mAh/g at 50  $\mu\text{A}$ . The capacity retention was very good up to 550 cycles at 200  $\mu\text{A}$ . Similar to  $\text{LiMn}_2\text{O}_4$ , vanadium oxide  $\text{V}_2\text{O}_5$  could also be lithiated by pulsing either  $\text{LiO}^t\text{Bu}$  and water or Lithd and ozone on top of the oxide film [90]. Using the Lithd and ozone precursors, lithium contents as high as 15 at% were obtained with only 100 cycles of the  $\text{Li}_2\text{CO}_3$  process applied on the 200 nm oxide film.

Lithium sulphide,  $\text{Li}_2\text{S}$ , is an attractive cathode material for high capacity lithium-sulphur batteries. It has recently been deposited by ALD [91] and requires inert atmosphere during sample handling to prevent reactions with ambient air, in a similar way to pure  $\text{Li}_2\text{O}$  [95].  $\text{Li}_2\text{S}$  has been deposited using  $\text{LiO}^t\text{Bu}$  and hydrogen sulphide between 150 and 300 °C. Unlike most lithium containing processes, this one produced a constant growth rate over the whole deposition temperature range studied. The refractive index of the films was much lower than the value for bulk crystalline  $\text{Li}_2\text{S}$ , indicating a lower density of the films. The films were amorphous and could not be crystallized with annealing in inert atmosphere. Both XRF (X-ray fluorescence) and XPS (X-ray photoelectron spectroscopy) gave a Li:S ratio of 2:1, with no carbon contamination in the  $\text{Li}_2\text{S}$  layer. Thus, the reaction between the precursors was very efficient. The  $\text{Li}_2\text{S}$  films produced high capacities of 800 mAh/g when deposited onto mesocarbon microbeads and a somewhat lower capacity of 500 mAh/g when deposited directly onto a 2D Cu current collector. In both cases the Coulombic efficiency was ~100%, indicating that the material could indeed be used as a cathode in lithium-sulphur batteries. However, film thickness had a large effect on the capacity, with thicker films producing smaller capacities per gram, as  $\text{Li}_2\text{S}$  is rather insulating. In addition, reactions with the copper current collector affected the charge-discharge profiles, indicating the formation of  $\text{Cu}_x\text{S}$ .

#### 4.2.2. Anodes

Table 5 presents examples of lithium-ion battery anode materials deposited by ALD. The selection of materials is quite a bit more limited than in the cathode case, most likely illustrating the consensus that improvements in battery energy density are more easily obtained with improved cathode materials. ALD-made  $\text{TiO}_2$  has been studied as an anode material mostly in various 3D-constructions, illustrating the conformal coating ability of ALD [78,96–98]. Using 3D-structures the areal capacity of the titania anode can be greatly improved [96,97] Generally,  $\text{TiO}_2$  can intercalate 0.5 Li, resulting in a capacity of 170 mAh/g [97] However, using nanomaterials more lithium can be intercalated and capacities of 330 mAh/g have been obtained with anatase nanotubes with a wall thickness of 5 nm [98]. These nanotubes also showed excellent capacity retention.

**Table 5.** Examples of conventional lithium-ion battery anode materials deposited by ALD. Abbreviations used:  $\text{O}^i\text{Pr}$  = *iso*-propoxide,  $\text{O}^t\text{Bu}$  = *tert*-butoxide, thd = 2,2,6,6-tetramethyl-3,5-heptanedionato, TPA = terephthalic acid, LiTP = lithium terephthalate.

Material	Precursors	$T_{\text{Dep}}$ (°C)	Growth Rate (Å)/Binary Cycle	Capacity (mAh/g)	Ref.
$\text{TiO}_2$	$\text{Ti}(\text{O}^i\text{Pr})_4 + \text{H}_2\text{O}$	160	0.33	330	[98]
$\text{Li}_x\text{Ti}_y\text{O}$	$\text{LiO}^t\text{Bu} + \text{Ti}(\text{O}^i\text{Pr})_4 + \text{H}_2\text{O}$	225, 250	0.7 with Li:Ti pulsing ratio 1:1	40	[99–101]
LiTP	Lithd + TPA	200–280	3.0 at 200 °C, decreases with $T_{\text{Dep}}$	350	[102]

Attempts on the deposition of lithium titanate spinel,  $\text{Li}_4\text{Ti}_5\text{O}_{12}$ , have been made using both titanium tetrachloride  $\text{TiCl}_4$  [99] and titanium tetra-*iso*-propoxide  $\text{Ti}(\text{O}^i\text{Pr})_4$  as precursors [99–101]. In both cases,  $\text{LiO}^t\text{Bu}$  was used as the lithium source and water was used as the oxygen source. Titanate

films deposited using  $\text{TiCl}_4$  reacted rapidly in air [99]. The films were amorphous as determined with X-ray diffraction and showed only very small amounts of lithium in ERDA measurements. In contrast, when using  $\text{Ti}(\text{O}^i\text{Pr})_4$  as the titanium source and applying a long pulse time for this precursor, uniform titanate films with higher lithium contents could be deposited [99]. These films also reacted with air, however the reaction was much slower than when using  $\text{TiCl}_4$  as the titanium precursor. The growth rate of the films did not depend much on the pulsing ratio of the two metal precursors, being approximately  $0.7 \text{ \AA}/\text{cycle}$  at  $225 \text{ }^\circ\text{C}$  [99]. In another report using the same precursors, the growth rate was said to be slightly different at  $0.6 \text{ \AA}/\text{cycle}$  at  $250 \text{ }^\circ\text{C}$  [100]. For the process at  $225 \text{ }^\circ\text{C}$ , ERDA measurements revealed that the lithium content of the films could be routinely tuned over a wide range by changing the metal pulsing ratio [99]. For example, with 33% lithium cycles the film stoichiometry was  $\text{Li}_{1.19}\text{TiO}_{2.48}$  and the carbon and hydrogen impurity contents were low. XPS and ERDA revealed that in this material lithium was enriched on the film surface, most likely forming a carbonate layer: carbonate peaks were visible both in FTIR (Fourier transform infrared spectroscopy) and XPS [99,101]. Despite the carbonate formation, the films showed the  $\text{Li}_4\text{Ti}_5\text{O}_{12}$  spinel phase in XRD measurements also in the as-deposited state. The crystallinity could be improved by annealing in nitrogen at  $640\text{--}700 \text{ }^\circ\text{C}$ . The annealed titanate films showed electrochemical activity but the capacity remained low at  $40 \text{ mAh/g}$  [101]. However, this low value might be related to uncertainties in the calculation of film mass. For the film deposited at  $250 \text{ }^\circ\text{C}$ , the Li:Ti ratio was reported as 2:1 with 44% lithium pulsing [100], which could indicate  $\text{Li}_2\text{TiO}_3$  formation—a well-known impurity phase for  $\text{Li}_4\text{Ti}_5\text{O}_{12}$  [103,104]. After annealing in argon at  $850$  and  $950 \text{ }^\circ\text{C}$  these films showed XRD peaks belonging to  $\text{Li}_4\text{Ti}_5\text{O}_{12}$  [100].

In addition to purely inorganic materials, ALD can also be used to deposit hybrid materials using organic molecules as the second precursor [105]. Lithium terephthalate (LiTP) has been deposited using Lithd and terephthalic acid as precursors between  $200$  and  $280 \text{ }^\circ\text{C}$  [102]. This material has been proposed as a possible Li-ion battery anode due to its high theoretical capacity of  $300 \text{ mAh/g}$  and a low potential of  $0.8 \text{ V}$  (vs.  $\text{Li}^+/\text{Li}$ ) [106]. The ALD process for LiTP showed saturation but no ALD window or constant growth rate as a function of the number of cycles [102]. The changing growth rate, accompanied by changes in the film density, could be related to the island growth mechanism of the film. The films were crystalline as deposited, which is unusual for ALD hybrid films. The films were electrochemically active and showed high rate capabilities with good capacity retention. The electrochemical properties of the films could further be enhanced by a protective LiPON layer on top of the electrode. The higher than theoretical capacity of  $350 \text{ mAh/g}$  is partly explained by difficulties in determining the electrode film thickness in electrochemical analyses. Recently, this anode material was combined with an organic cathode material dilithium-1,4-benzenediolate to produce a functioning atomic layer/molecular layer deposited thin film battery [107].

#### 4.2.3. Solid Electrolytes

ALD has showcased its versatility in the deposition of potential solid electrolytes for lithium-ion batteries (Table 6). Many materials, both crystalline and amorphous, have been deposited and ionic conductivities of the order of  $10^{-7} \text{ S/cm}$  have been obtained with various materials. Of the traditional solid electrolytes, LiPON has been deposited using both ALD and PEALD [108,109].

**Table 6.** Examples of potential solid lithium-ion battery electrolyte materials deposited by ALD. Abbreviations used: LiHMDS = lithium hexamethyldisilazide, LiTMSO = lithium trimethyl silanolate,  $\text{O}^t\text{Bu}$  = *tert*-butoxide, TEOS = tetraethyl orthosilicate, TMPO = trimethyl phosphate, DEPA = diethyl phosphoramidate, OEt = ethoxide, thd = 2,2,6,6-tetramethyl-3,5-heptanedionato, TMA = trimethyl aluminum,  $\text{La}(\text{FMAD})_3$  = lanthanum tris(*N,N*-di-*iso*-propylformamidinate), TDMAZ = tetrakis(dimethylamido)zirconium, TDMA-Al = tris(dimethylamido) aluminum, HF-py = mixture of HF and pyridine.

Material	Precursors	$T_{\text{Dep}}$ (°C)	Growth Rate (Å)/Binary Cycle	Ionic Conductivity (S/cm)	Ref.
$\text{Li}_x\text{Si}_y\text{O}$	LiHMDS + $\text{O}_3$	150–400	Varies with temperature	Not measured	[110,111]
	LiTMSO + $\text{O}_3$ + $\text{H}_2\text{O}$	175–300	1.5 at 200–300 °C	Not measured	[112]
	$\text{LiO}^t\text{Bu}$ + TEOS + $\text{H}_2\text{O}$	225–300	0.5 at 250 °C	$10^{-10}$ – $10^{-9}$ at 30 °C	[113]
$\text{Li}_3\text{PO}_4$	$\text{LiO}^t\text{Bu}$ + TMPO	225–300 [114] 250–350 [115]	0.7 at 225–275 °C [114], 0.69 at 300 °C [115]	$10^{-8}$ – $10^{-7}$ at RT [115,116]	[114–116]
LiPON	LiHMDS + DEPA	250–350	0.7 at 270–310 °C	$6.6 \times 10^{-7}$ at RT (9.7 at.% nitrogen)	[108]
	$\text{LiO}^t\text{Bu}$ + $\text{H}_2\text{O}$ + TMPO + $\text{N}_2$ plasma	250	1.05	$1.45 \times 10^{-7}$ (5.5 at.% nitrogen, increases with nitrogen contents)	[109]
$\text{Li}_x\text{Ta}_y\text{O}$	$\text{LiO}^t\text{Bu}$ + $\text{Ta}(\text{OEt})_5$ + $\text{H}_2\text{O}$	225	0.7 with Li:Ta pulsing ratio 1:6.	$1.2 \times 10^{-8}$ at RT	[117]
$\text{Li}_x\text{Nb}_y\text{O}$	LiHMDS + $\text{Nb}(\text{OEt})_5$ + $\text{H}_2\text{O}$	235	~0.64 with Li:Nb pulsing ratio 1:2	Not measured	[118]
	$\text{LiO}^t\text{Bu}$ + $\text{Nb}(\text{OEt})_5$ + $\text{H}_2\text{O}$	235	~0.68 with Li:Nb pulsing ratio 1:2	$6.4 \times 10^{-8}$ at 30 °C	[119]
$\text{Li}_x\text{La}_y\text{Ti}_z\text{O}$	$\text{LiO}^t\text{Bu}$ + $\text{La}(\text{thd})_3$ + $\text{TiCl}_4$ + $\text{O}_3$ + $\text{H}_2\text{O}$	225	Varies with pulsing ratio	Not measured.	[120]
$\text{Li}_x\text{Al}_y\text{Si}_z\text{O}$	$\text{LiO}^t\text{Bu}$ + TMA + TEOS + $\text{H}_2\text{O}$	290	1.0 with Li:Al pulsing ratio 6:10	$10^{-9}$ – $10^{-7}$ at RT, depends on Li contents	[121]
$\text{Li}_x\text{La}_y\text{Zr}_z\text{O:Al}$	$\text{LiO}^t\text{Bu}$ + $\text{La}(\text{FMAD})_3$ + TDMAZ + TMA + $\text{O}_3$	225	1.0 with Li:La:Zr:Al ratio 8:28:12:1	$1 \times 10^{-8}$ at RT for amorphous film	[122]
$\text{Li}_x\text{Al}_y\text{S}$	$\text{LiO}^t\text{Bu}$ + TDMA-Al + $\text{H}_2\text{S}$	150	0.5 with Li:Al ratio 1:1	$2.5 \times 10^{-7}$ at RT	[123]
$\text{Li}_x\text{Al}_y\text{F}$	LiHMDS + TMA + HF-py	150	0.45 with Li:Al pulsing ratio 1:1	$7.5 \times 10^{-6}$ at RT	[51]
	$\text{LiO}^t\text{Bu}$ + $\text{AlCl}_3$ + $\text{TiF}_4$	250	1 with Li:Al pulsing ratio 1:1	$(3.5 \pm 0.5) \times 10^{-8}$ at RT	[124]

Lithium silicates can have reasonably high lithium-ion conductivities, especially in the amorphous state [125–127]. The silylamide precursor LiHMDS (lithium hexamethyldisilazide) provides a convenient route to lithium silicate deposition when combined with ozone [110,111]. The process exhibited good ALD behaviour at 250 °C, with saturation of both precursors seen and the film thickness increased linearly with the number of cycles. However, no ALD window was present and instead the growth rate increased from approximately 0.3 Å/cycle at 150 °C to 1.7 Å/cycle at 400 °C. This increase was explained with subsequent reaction mechanism studies [111]. The HMDS-ligand of the metal precursor reacts with surface hydroxyl groups, decomposing to different side products. Some of these side products are unreactive in the process but can still block active sites from the desired  $-\text{Si}(\text{CH}_3)_3$  groups. At higher temperatures, the decomposition of the ligand to  $-\text{Si}(\text{CH}_3)_3$  is enhanced and in addition desorption of unreactive products is faster. The deposited films were amorphous below 400 °C and showed only small amounts of carbon and hydrogen impurities, as determined by ERDA [110]. Notably, no nitrogen was detected in the film despite the lithium precursor being a silylamide. The Li:Si and Si:O ratios changed with deposition temperature but at 250 °C the film composition was  $\text{Li}_2\text{SiO}_{2.9}$  which is very close to the lithium metasilicate  $\text{Li}_2\text{SiO}_3$ . The ionic conductivity of these films was not measured.

Recently, lithium silicates have been deposited also using LiTMSO (lithium trimethyl silanolate) [112] and lithium *tert*-butoxide [113]. With LiTMSO, to obtain good quality films both an ozone and a water pulse were needed after the metal precursor pulse [112]. It was postulated that the water generates hydroxyl groups on the surface of the silicate film, which are beneficial for the adsorption of LiTMSO. All the films were amorphous and the growth rate remained constant at 1.5 Å/cycle between 200 and 300 °C. Films deposited at low temperatures had significant hydrogen contents of 14 at.%. The amounts of both lithium and silicon increased with increasing deposition temperatures while the levels of impurities decreased but the Li:Si ratio remained at 2:1. No ionic conductivity information is available for these films.

Lithium *tert*-butoxide could deposit lithium silicates in combination with TEOS (tetraethyl orthosilicate) and water [113]. For these films, a Li:Si ratio close to  $\text{Li}_4\text{SiO}_4$  was obtained at all deposition temperatures. The ionic conductivity of these films was quite low, reaching a maximum of  $5 \times 10^{-9}$  S/cm in films deposited at 250 °C.

LiPON, currently the most often used solid lithium-ion electrolyte material, was undoubtedly the stimulus for the ALD studies on lithium phosphate films.  $\text{Li}_3\text{PO}_4$  can be deposited using either  $\text{LiO}^t\text{Bu}$  or LiHMDS as the lithium source and TMPO (trimethyl phosphate, Figure 9) as the phosphate precursor [114,115]. The  $\text{LiO}^t\text{Bu}$  + TMPO process showed a constant growth rate of approximately 0.7 Å/cycle between 225 and 275 °C [114]. However, no complete saturation was observed. The films were slightly crystalline and showed decreasing impurity levels at higher deposition temperatures in ERDA measurements. At 300 °C, the film composition was  $\text{Li}_{2.6}\text{PO}_{3.7}$ . The process utilizing LiHMDS is less than ideal, as the film growth rate varies strongly with deposition temperature, being 0.4 Å/cycle at 275 °C and 1.3 Å/cycle at 350 °C. At 300 °C, these films were close to stoichiometric lithium phosphate, being  $\text{Li}_{2.8}\text{PO}_{3.9}$  as determined by ERDA. However, using LiHMDS as the lithium precursor led to higher carbon and hydrogen impurities than the  $\text{LiO}^t\text{Bu}$  process. Regardless of the lithium precursor, the phosphate films crystallized into the orthorhombic  $\text{Li}_3\text{PO}_4$  phase during HTXRD measurements.

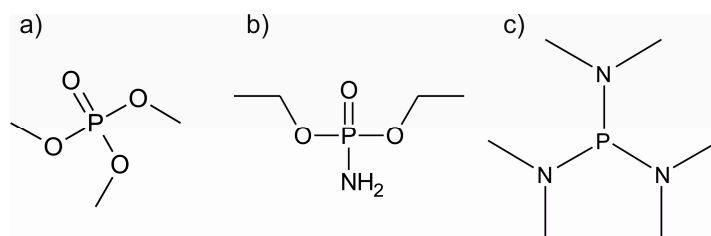


**Figure 9.** The structures of three phosphorus precursors used to deposit lithium phosphate and LiPON. (a) TMPO, or trimethyl phosphate; (b) DEPA, or diethyl phosphoramidate; (c) TDMAP, or *tris*(dimethylamino)phosphine.

Wang et al. [115] and Létiche et al. [116] have studied the  $\text{Li}_3\text{PO}_4$  process using  $\text{LiO}^t\text{Bu}$  and TMPO in an effort to measure the lithium-ion conductivity of these films. Wang et al. reported an increasing growth rate as a function of the deposition temperature at 250–325 °C, which might be a result of the somewhat unsaturative behaviour of the process [114]. Electrochemical impedance spectroscopy showed that the films had rather good conductivities when deposited at 300 °C:  $3.3 \times 10^{-8}$  S/cm was extrapolated for a film with a composition of  $\text{Li}_{2.8}\text{PO}_z$  (as determined by XPS) [115]. Similarly, Létiche et al. reported conductivities as high as  $4.3 \times 10^{-7}$  S/cm for  $\text{Li}_3\text{PO}_4$  deposited at 300 °C [116]. These results are rather surprising, as it is common knowledge that lithium phosphate is generally no match for its nitrogen-doped counterpart LiPON and its conductivities of  $10^{-8}$ – $10^{-6}$  S/cm [32]. It appears that small film thicknesses can play a role in these high ionic conductivities [116].  $\text{Li}_3\text{PO}_4$  layers have been studied in contact with electrode materials [128,129] and it has been found that although the phosphate layer can decrease the electrode capacity, capacity retention is improved due to decreased transition metal dissolution and more stable SEI formation [128].

Recently, the deposition of LiPON was achieved both by thermal and plasma-enhanced ALD [108,109,130]. In the PEALD process, LiO<sup>t</sup>Bu was used as the lithium source combined with a pulsing sequence of water, TMPO and nitrogen plasma [109]. Deposition of Li<sub>2</sub>O/LiOH before exposure to TMPO resulted in less carbon impurities as compared to the process used by Hämäläinen et al. for Li<sub>3</sub>PO<sub>4</sub> [114]. By using nitrogen plasma after the TMPO pulse, nitrogen could be incorporated into the films, causing the amorphization of the crystalline Li<sub>3</sub>PO<sub>4</sub>. In the thermal ALD process, the problems of nitrogen incorporation and nitrogen-phosphorous bond formation were resolved by using diethyl phosphoramidate, DEPA, a phosphate precursor with an amine group (Figure 9) [108]. By using DEPA with LiO<sup>t</sup>Bu, nitrogen contents as high as 9.7 at.% were achieved. However, the thermal ALD process led to high carbon impurities from 9.9 to 13.3 at.% compared to virtually none in the PEALD process [109]. Both processes deposited conformal coatings on demanding substrates as required from a potential solid electrolyte material. In addition, very good electrochemical properties were realized with ionic conductivities of  $1.45 \times 10^{-7}$  S/cm for the PEALD process (5 at.% nitrogen) and  $6.6 \times 10^{-7}$  S/cm for the thermal ALD process (9.7 at.% nitrogen) [108,109]. The plasma-deposited LiPON has already been studied as a protecting layer for a conversion lithium-ion battery electrode. It was found that the LiPON layer enhanced the capacity retention of the electrode by providing both a high lithium-ion conductivity and mechanical support during cycling [131].

The most recent addition to the ALD LiPON processes was reported by Shibata, using TDMAP or *tris*(dimethylamino)phosphine (Figure 9) as the phosphorous source, LiO<sup>t</sup>Bu as the lithium source and O<sub>2</sub> and NH<sub>3</sub> for oxidation and nitrification [130]. The high process temperatures of over 400 °C raise concerns of more CVD- than ALD-type film growth, especially combined with the changing growth rate as a function of cycles. However, no carbon impurities were found in the films with XPS. The N contents varied between 2 and 6 at.% and an ionic conductivity of  $3.2 \times 10^{-7}$  at 25 °C was obtained for these films.

Lithium tantalate, similarly to lithium niobate, is an interesting ferroelectric material [132,133]. Its amorphous form has also been suggested as a possible solid electrolyte material for lithium ions [117,134,135]. The material has been deposited by ALD using LiO<sup>t</sup>Bu, Ta(OEt)<sub>5</sub> and water as precursors at 225 °C [117]. The film growth rate changed depending on the cycle ratio of the two binary processes, being 0.74 Å/binary cycle with a 1Li<sub>2</sub>O + 6Ta<sub>2</sub>O<sub>5</sub> pulsing sequence. Similarly, the lithium contents of the films changed drastically with pulsing ratio (Figure 10). Both XANES (X-ray absorption near edge structure) and XPS measurements revealed that the chemical environment of tantalum in the films was similar to that of tantalum in stoichiometric LiTaO<sub>3</sub>. However, in the films deposited with the highest tantalum oxide pulsing ratios there were also some indications of a Ta<sub>2</sub>O<sub>5</sub> phase. XPS also revealed some carbonate formation on the film surface. Less carbonate was formed on the surface of films deposited with high numbers of tantalum oxide subcycles, indicating that Ta<sub>2</sub>O<sub>5</sub> was offering some protection for the lithium in the film against reactions with carbon dioxide in air. A lithium tantalate film with a composition of Li<sub>5.1</sub>TaO<sub>x</sub> was studied with electrochemical impedance spectroscopy (EIS) [117]. The film showed a room temperature lithium-ion conductivity of  $1.2 \times 10^{-8}$  S/cm, which increased to  $9.0 \times 10^{-7}$  S/cm at 100 °C. The material has later been used as a protective layer on lithium nickel cobalt manganese oxide cathodes [135]. With 5 supercycles of LiTaO<sub>3</sub> (metal oxide pulsing ratio Li:Ta = 1:6), enhancements in both electrode capacity and cycling ability were obtained. Recently, LiTaO<sub>3</sub> films were also made using ALD and solid state reactions: Li<sub>2</sub>CO<sub>3</sub> was deposited from Lithd and O<sub>3</sub> onto amorphous ALD-Ta<sub>2</sub>O<sub>5</sub> and upon annealing at 750 °C in air crystalline LiTaO<sub>3</sub> was formed with low impurity levels and a Li:Ta ratio of 1.5:1 [104]. The ionic conductivity of this film has not been measured but it can be expected to remain small due to both the crystalline structure of the film and its close-to-stoichiometric content of lithium.

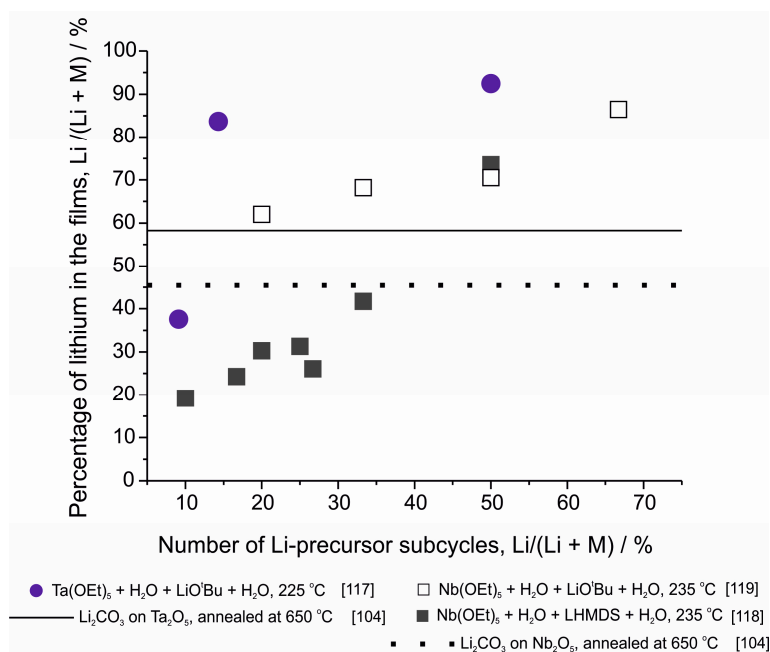


**Figure 10.** The amount of lithium cations deposited into lithium tantalate and lithium niobate films as a function of the amount of lithium containing subcycles. Data points obtained from [117–119]. The solid line represents the stoichiometry obtained for the lithium tantalate deposited by using 3000 cycles of Lithd and O<sub>3</sub> on 50 nm of Ta<sub>2</sub>O<sub>5</sub> in Ref. [104]. The dashed line represents the stoichiometry obtained for the lithium niobate deposited by using same conditions but on Nb<sub>2</sub>O<sub>5</sub> film in Ref. [104]. For stoichiometric LiTaO<sub>3</sub> and LiNbO<sub>3</sub>, the lithium content is 50%.

Similar to lithium tantalate, lithium niobate thin films have also been deposited by ALD [118,119]. In the first paper, LiNbO<sub>3</sub> was deposited using Nb(OEt)<sub>5</sub>, LiHMDS and water as precursors [118]. This work focused on the evolution of the lithium content in the films (Figure 10), on the epitaxial growth of the film on various surfaces and on the ferroelectric properties of the films. Later, the material was also deposited with LiO<sup>t</sup>Bu as the lithium source [119]. It is interesting to note that while the two processes use different lithium precursors, they produce films with the same stoichiometry when the pulsing sequence is Li:Nb = 1:1 (Figure 10). For other pulsing ratios, the LiO<sup>t</sup>Bu process seems to produce much higher lithium contents but this might be an artefact caused by the differing analysis methods used in these reports, XPS [119] and ToF-ERDA [118]. For the LiO<sup>t</sup>Bu process, the films with the lowest lithium contents showed the highest ionic conductivity of  $6.4 \times 10^{-8}$  S/cm at 30 °C [119]. In addition to these reports, LiNbO<sub>3</sub> has also been made with the same combination of ALD and solid state reactions as was mentioned for LiTaO<sub>3</sub> [104]. In this case also the post-deposition annealing of a bilayer of Li<sub>2</sub>CO<sub>3</sub> and Nb<sub>2</sub>O<sub>5</sub> produced a film with low impurity content. However, compared to the LiTaO<sub>3</sub> case, here the films were slightly lithium deficient (Figure 10).

The first truly quaternary lithium material deposited by ALD was lithium lanthanum titanate (LLT), reported by Aaltonen et al. in 2010 [120]. Thin films were deposited by combining binary ALD processes for TiO<sub>2</sub>, La<sub>2</sub>O<sub>3</sub> and Li<sub>2</sub>O/LiOH and were amorphous as deposited. In that work TiCl<sub>4</sub> was used as the titanium precursor and it was found that applying the Li<sub>2</sub>O/LiOH subcycle after the TiO<sub>2</sub> cycle resulted in rougher and less uniform films than when lithium was pulsed after the La<sub>2</sub>O<sub>3</sub> subcycle. This is a clear indication that the pulsing order can have a large effect on the deposition of quaternary materials. As reactivity problems were also observed in the deposition of lithium titanate using TiCl<sub>4</sub> [99], the chloride precursor might be playing a large, thus far unknown role in these processes. These problems could be related to LiCl formation, for example. For the LLT deposition, a pulse sequence where 3 cycles of La<sub>2</sub>O<sub>3</sub> were applied after one TiO<sub>2</sub> cycle and the number of lithium subcycles was varied, was used. The content of lithium in the film did not linearly

follow the number of  $\text{Li}_2\text{O}/\text{LiOH}$  subcycles. This could mean that the reactivity of  $\text{LiO}^t\text{Bu}$  is lower on a  $\text{Li}_2\text{O}/\text{LiOH}$  surface compared to its reactivity on a  $\text{La}_2\text{O}_3$  surface, a somewhat similar conclusion as was made in the deposition experiments on lithium aluminate [136]. Nevertheless, saturation as a function of the  $\text{LiO}^t\text{Bu}$  pulse length was observed [120]. The maximum lithium content reached with this pulsing scheme was approximately 20 at.%. The lanthanum content stayed constant in all experiments but the content of titanium decreased as a function of the increased lithium content. Under saturative conditions the film composition, as determined by ToF-ERDA, was  $\text{Li}_{0.32}\text{La}_{0.30}\text{TiO}_z$ . Interestingly, SIMS (secondary ion mass spectrometry) depth profiling seemed to indicate that lithium was somewhat concentrated onto the film-substrate interface, whereas in many cases lithium has been reported to preferably reside on the outer surface of the film [99,118]. However, this observation could be an artefact caused by sputtering during SIMS. The films could be crystallized by annealing in oxygen. The XRD diffractograms matched well with the reported peak positions of  $\text{Li}_{0.33}\text{La}_{0.557}\text{TiO}_3$ , however four peaks could not be identified [120].

$\text{Li}_x\text{Al}_y\text{Si}_z\text{O}$ , another amorphous solid electrolyte, has been studied by Perng et al. [121]. The material belongs to the lithium aluminosilicate family, which includes materials with high lithium-ion conductivities with various metal ratios [30]. Lithium aluminosilicate was deposited by ALD using a pulsing sequence of  $\text{Al}_2\text{O}_3$  from TMA and water,  $\text{Li}_2\text{O}/\text{LiOH}$  from  $\text{LiO}^t\text{Bu}$  and water and  $\text{SiO}_2$  from TEOS and water [121]. With a pulsing sequence of Al:Li:Si = 10:6:4 the film thickness increased linearly with the number of supercycles. The lithium contents of the films, as determined by synchrotron ultraviolet photoemission spectroscopy (UPS), increased with increasing lithium oxide pulsing ratio but showed quite a lot of scattering (Figure 11). The deposited films were shown to be pinhole free and had ionic conductivities between  $10^{-9}$  and  $10^{-7}$  S/cm at room temperature, depending on the lithium content. Higher lithium contents led to higher conductivities but also increased the activation energy. It should be noted that the film thicknesses used in these experiments were very small, 10 nm and below. Larger thicknesses led to a lower ionic conductivity.

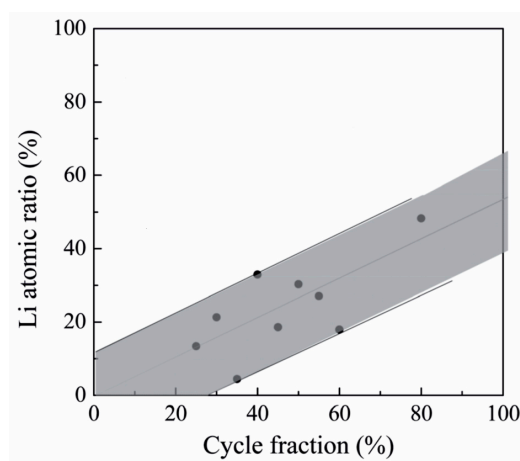


**Figure 11.** The lithium content in lithium aluminosilicate films as a function of the  $\text{Li}_2\text{O}$  cycle fraction  $a/(a + b + c)$ , as determined from synchrotron UPS spectra. Adapted with permission from [121]. Copyright 2014 The Royal Society of Chemistry.

Kazyak et al. have taken on the impressive task of depositing the garnet oxide  $\text{Li}_7\text{La}_3\text{Zr}_2\text{O}_{12}$  by ALD [122]. This crystalline material is known to have a lithium-ion conductivity close to  $10^{-3}$  S/cm at room temperature [137]. In order to stabilize the desired cubic phase at room temperature, the material was doped with alumina [122]. This resulted in an ALD process combining 8 subcycles of  $\text{Li}_2\text{O}$ , 28 subcycles of  $\text{La}_2\text{O}_3$ , 12 subcycles of  $\text{ZrO}_2$  and 1  $\text{Al}_2\text{O}_3$  subcycle at 225 °C to obtain an amorphous film with metal ratios Li:La:Zr:Al = 52:27:19:2 (ideal composition 54:26:17:2). Interestingly, despite using ozone as the oxygen source for all subcycles, no  $\text{Li}_2\text{CO}_3$  or  $\text{La}_2(\text{CO}_3)_3$  formation was evident

from XPS results. The thickness of the films increased linearly with the number of supercycles and good conformality was also obtained. The ionic conductivity of the as-deposited, amorphous film was  $1.2 \times 10^{-6}$  S/cm at 100 °C and did not differ between in-plane and through-plane measurements. By extrapolation, the conductivity was  $10^{-8}$  S/cm at RT. The films could be crystallized to the cubic  $\text{Li}_7\text{La}_3\text{Zr}_2\text{O}_{12}$  phase with annealing at 555 °C in inert atmosphere. A lithium-excess in the film and an extra lithium source were needed during the annealing due to lithium loss from the film. The annealed films had an island morphology, which prevented reliable conductivity measurements.

Although the majority of published ternary lithium ALD processes are for oxide materials, sulphides and fluorides have been studied as well [51,123]. Lithium aluminum sulphide  $\text{Li}_x\text{Al}_y\text{S}$  has been deposited using subcycles of  $\text{Li}_2\text{S}$  [91] ( $\text{LiO}^t\text{Bu} + \text{H}_2\text{S}$ ) and  $\text{Al}_2\text{S}_3$  [138] (tris(dimethylamido)aluminum(III) +  $\text{H}_2\text{S}$ ). Using a 1:1 subcycle ratio resulted in a Li:Al ratio of 2.9:1 in films deposited at 150 °C, as determined with ICP-MS (inductively coupled plasma mass spectrometry) [123]. Evaluation of the metal ratio from QCM (quartz crystal microbalance) data, assuming stoichiometric growth, resulted in a metal ratio of 3.5:1 which is reasonably close to the value from ICP-MS. The ternary sulphide growth was linear as a function of cycles, with a reported growth rate of 0.50 Å/cycle. The growth rate during the  $\text{Li}_2\text{S}$  subcycle seemed somewhat lower in the ternary process than the one reported for the binary process [91]. This difference was not commented on in ref. [123] but it most likely originates from different starting surfaces. A 50 nm  $\text{Li}_x\text{Al}_y\text{S}$  film was measured to have a room temperature ionic conductivity of  $2.5 \times 10^{-7}$  S/cm, which is among the best quoted conductivities of ALD-made films [108,109,117,121,123]. The sulphide was studied as an artificial SEI-layer on metallic Li and it was found to effectively stabilize the interface between the metal anode and an organic liquid electrolyte [123]. In addition, the coating decreased lithium metal dendrite formation during cycling, which considerably improves the safety of lithium metal anodes.

Multicomponent, lithium-containing fluorides have not been studied extensively by ALD [51,124,139]. Still,  $\text{Li}_3\text{AlF}_6$ , has been deposited using multiple processes. This material will be discussed in the next section on fluoride deposition using ALD.

## 5. Atomic Layer Deposition of Metal Fluorides

Metal fluorides have been of interest to ALD chemists since the beginning of the 1990s. In the very beginning, doping of electroluminescent materials with fluorine was studied [140] and soon after the first report on depositing  $\text{CaF}_2$ ,  $\text{ZnF}_2$  and  $\text{SrF}_2$  was published [141]. For the first two decades, metal fluorides were studied mainly because of their optical properties, namely low refractive indices and low absorption in the UV range [142]. However, with the rise of lithium-ion battery related ALD research, the potential of ALD metal fluorides in batteries has also been recognized [51,143–145]. Still, very few results on using atomic layer deposited metal fluoride thin films in lithium-ion batteries is available at this time.

Table 7 summarizes all reported ALD fluoride processes. Electrochemical analysis results are reported when available. The processes are divided into sections based on the fluorine precursor used. The materials are listed in the order of main groups followed by transition metals and lanthanides in the order of atomic numbers. For discussion purposes, a somewhat historical approach has been taken in the following subchapters. Besides this review, ALD of metal fluorides has been discussed in the academic dissertations of Pilvi [142], Lee [146] and Mäntymäki [79].

**Table 7.** ALD processes reported for fluoride materials. Abbreviations used: LiHMDS = lithium hexamethyldisilazide, HF-py = mixture of HF and pyridine, EtCp = ethylcyclopentadienyl, thd = 2,2,6,6-tetramethyl-3,5-heptanedionato, TMA = trimethyl aluminum, Ac = acetate, DEZ = diethylzinc, TEMAZ = tetrakis(ethylmethylamido) zirconium, O<sup>t</sup>Bu = *tert*-butoxide, TDMAH = tetrakis(dimethylamido) hafnium, hfac = 1,1,1,5,5,5-hexafluoro-2,4-pentanedionato.

Material	Precursors	T <sub>Dep</sub> (°C)	Growth Rate (Å)/Cycle	Ref.
Fluorides Using HF as the Fluorine Precursor				
LiF	LiHMDS + HF-py	150	0.5	[147]
MgF <sub>2</sub>	Mg(EtCp) <sub>2</sub> + HF-py	150	0.4	[147]
MgF <sub>2</sub>	Mg(EtCp) <sub>2</sub> + HF	100–250	Varies, 0.6 at 100 °C	[148]
CaF <sub>2</sub>	Ca(thd) <sub>2</sub> + HF/NH <sub>4</sub> F	300–400	0.2 at 320–400 °C	[141]
SrF <sub>2</sub>	Sr(thd) <sub>2</sub> + HF/NH <sub>4</sub> F	260–320	Varies, 0.6 at 300 °C	[141]
AlF <sub>3</sub>	TMA + HF-py	75–300	Varies, 1.0 at 150 °C	[143]
AlF <sub>3</sub>	TMA + HF	100–200	Varies, 1.2 at 100 °C	[149]
MnF <sub>2</sub>	Mn(EtCp) <sub>2</sub> + HF-py	150	0.4	[147]
ZnF <sub>2</sub>	Zn(Ac) <sub>2</sub> ·2H <sub>2</sub> O + HF/NH <sub>4</sub> F	260–320	0.7 at 260–300 °C	[141]
ZnF <sub>2</sub>	DEZ + HF-py	150	0.7	[147]
ZrF <sub>4</sub>	TEMAZ + HF-py	150	0.9	[147]
ZrF <sub>4</sub>	Zr(O <sup>t</sup> Bu) <sub>4</sub> + HF-py	150	0.6	[147]
HfF <sub>4</sub>	TDMAH + HF-py	150	0.8	[147]
Li <sub>x</sub> Al <sub>y</sub> F	LiHMDS + TMA + HF-py	150	0.45 with Li:Al pulsing ratio 1:1	[51,146]
Fluorides Using Metal Fluorides as the Fluorine Precursor				
LiF	Lithd + TiF <sub>4</sub>	250–350	1.0 at 325 °C	[150]
LiF	Mg(thd) <sub>2</sub> + Lithd + TiF <sub>4</sub>	300–350	1.4 at 325 °C	[151]
LiF	LiO <sup>t</sup> Bu + WF <sub>6</sub>	150–300	–	[152]
LiF	LiO <sup>t</sup> Bu + MoF <sub>6</sub>	150–300	2.6	[152]
LiF	LiO <sup>t</sup> Bu + TiF <sub>4</sub>	200–300	0.5 at 250 °C	[124]
MgF <sub>2</sub>	Mg(thd) <sub>2</sub> + TiF <sub>4</sub>	250–400	Varies, 1.6 at 250 °C	[153]
MgF <sub>2</sub>	Mg(thd) <sub>2</sub> + TaF <sub>5</sub>	225–400	Varies, 1.1 at 225–250 °C	[154]
CaF <sub>2</sub>	Ca(thd) <sub>2</sub> + TiF <sub>4</sub>	300–450	Varies, 1.6 at 300–350 °C	[155]
AlF <sub>3</sub>	AlCl <sub>3</sub> + TiF <sub>4</sub>	160–340	Varies, 0.75 at 240 °C	[156]
AlF <sub>3</sub>	TMA + TaF <sub>5</sub>	125–350	Varies, 1.9 at 125 °C	[145]
YF <sub>3</sub>	Y(thd) <sub>3</sub> + TiF <sub>4</sub>	175–325	Varies, 1.3–1.5 at 200–300 °C	[157]
LaF <sub>3</sub>	La(thd) <sub>3</sub> + TiF <sub>4</sub>	225–350	Varies, 5.2 at 225–250 °C	[158]
Li <sub>x</sub> Al <sub>y</sub> F	LiF + Al(thd) <sub>3</sub> + TiF <sub>4</sub>	250–350	–	[139]
Li <sub>x</sub> Al <sub>y</sub> F	LiO <sup>t</sup> Bu + AlCl <sub>3</sub> + TiF <sub>4</sub>	250	1	[124]
AlW <sub>x</sub> F <sub>y</sub>	TMA + WF <sub>6</sub>	200	1–1.5	[144,159]
Fluorides Using Other Processes				
LiF	MgF <sub>2</sub> + Lithd	275–325	–	[151]
MgF <sub>2</sub>	Mg(thd) <sub>2</sub> + Hhfac + O <sub>3</sub>	–	0.38	[160]
CaF <sub>2</sub>	Ca(hfac) <sub>2</sub> + O <sub>3</sub>	300	0.3	[160]
CaF <sub>2</sub>	Ca(thd) <sub>2</sub> + Hhfac + O <sub>3</sub>	250–350	0.4	[160]
AlF <sub>3</sub>	TMA + SF <sub>6</sub> plasma	50–300	Varies, 0.85 at 200 °C	[161]
LaF <sub>3</sub>	La(thd) <sub>3</sub> + Hhfac + O <sub>3</sub>	–	0.49	[160]
Li <sub>x</sub> Al <sub>y</sub> F	AlF <sub>3</sub> + Lithd	250–300	–	[139]

### 5.1. ALD of Metal Fluorides Using HF as the Fluorine Source

ZnF<sub>2</sub>, SrF<sub>2</sub> and CaF<sub>2</sub> films, reported in the first paper on ALD of fluorides in 1994, were deposited using HF as the fluorine source [141]. The HF gas was generated in the reactor in situ by thermal decomposition of ammonium fluoride, NH<sub>4</sub>F. Thus, there was no need to store and handle large amounts of gaseous HF. An added benefit of this method was that excess HF can be condensed again inside the reactor as ammonium fluoride, without the gas entering and damaging the vacuum pump. Metal thd-complexes were used as precursors for strontium and calcium and zinc fluoride was deposited using zinc acetate. All the films were close to stoichiometric and polycrystalline, with carbon

impurities of the order of 0.5 at.%. For the calcium and strontium fluoride processes, the growth rates decreased with increasing deposition temperatures (Figure 12b).

The work on fluoride deposition using HF has been continued by many groups, including Hennessy et al., who have deposited magnesium and aluminum fluoride films using anhydrous HF with bis(ethylcyclopentadienyl)magnesium and TMA as metal precursors [148,149]. Magnesium fluoride is an interesting material due to its large band gap and low refractive index [142,153]. Aluminum fluoride is a material with a similar variety of possible optical applications [149,162–164]. In addition, as already mentioned,  $\text{AlF}_3$  is a potential artificial SEI-layer for protecting both cathodes and anodes [47,143,145,165–167]. Thus,  $\text{AlF}_3$  has become a much studied ALD material in the past few years [143,145,147,149,156]. Magnesium fluoride showed growth rates of 0.6 to 0.3 Å/cycle in the deposition temperature range of 100 to 250 °C (Figure 12a) [148].  $\text{AlF}_3$  showed a similar decrease in growth rate, being 1.2 Å/cycle at 100 °C and 0.5 Å/cycle at 200 °C (Figure 12c) [149].  $\text{MgF}_2$  films were crystalline and showed small amounts of carbon and oxygen impurities and a slight fluorine deficiency in XPS measurements (Figure 12d) [148].  $\text{AlF}_3$  films were amorphous, with 1–2 at.% of oxygen [149]. The aluminum fluoride films were stoichiometric based on XPS measurements. The anhydrous HF required an unconventionally long purging time to obtain good film uniformity. It was speculated that multilayer physisorption might be the cause of this effect. However, it has been reported in another publication that  $\text{MgF}_2$  does not readily adsorb HF during the ALD growth process [147].

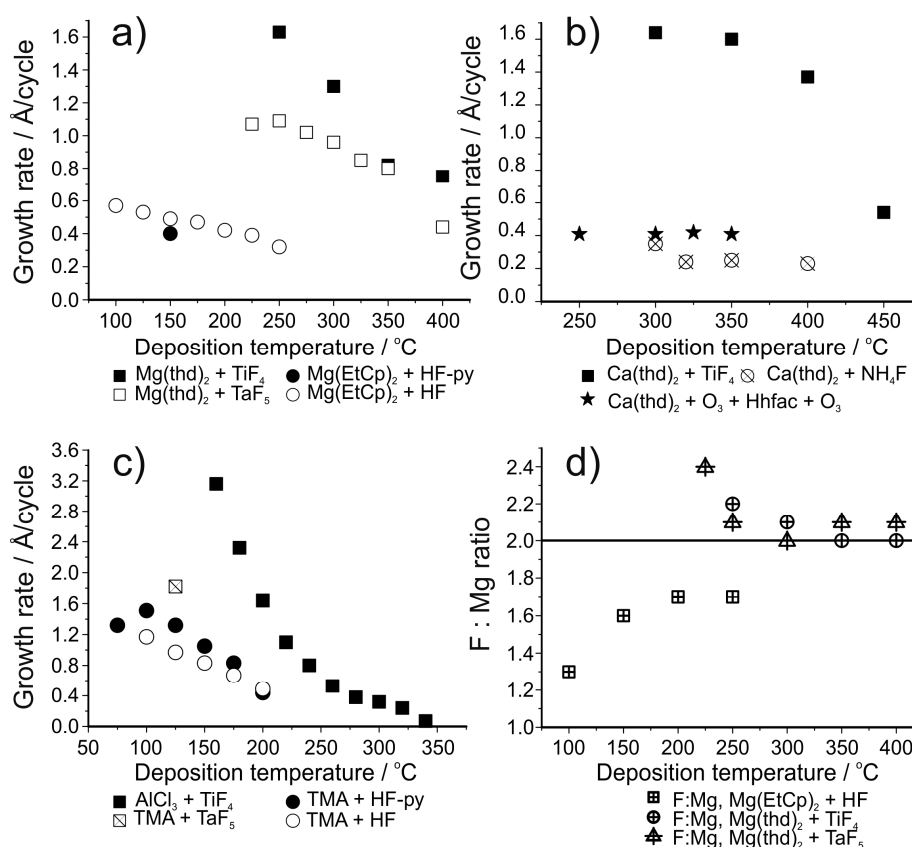


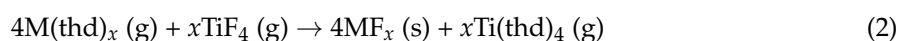
**Figure 12.** (a) Growth rates of  $\text{MgF}_2$  films as a function of deposition temperature using different precursor combinations; (b) Growth rates of  $\text{CaF}_2$  films as a function of deposition temperature using different precursor combinations; (c) Growth rates of  $\text{AlF}_3$  films as a function of deposition temperature using different precursor combinations; (d) F-Mg ratios of  $\text{MgF}_2$  films deposited at different temperatures and with different precursor combinations. The HF-process was analysed with XPS and the  $\text{TiF}_4$  and  $\text{TaF}_5$  processes with ERDA. Data obtained from References: (a) [147,148,153,154]; (b) [141,155,160]; (c) [143,145,149,156]; (d) [148,153,154].

A number of metal fluorides have recently been deposited by Lee et al. using HF, including  $\text{AlF}_3$  [143],  $\text{LiF}$ ,  $\text{ZrF}_4$ ,  $\text{ZnF}_2$  and  $\text{MgF}_2$  [147]. Of these materials, lithium fluoride is of special interest because of its band gap of approximately 14 eV and low refractive index of 1.39 at 580 nm, much like  $\text{AlF}_3$  as discussed previously [168,169]. For the deposition of these fluorides, HF was generated from a solution containing 30 wt.% of pyridine and 70 wt.% HF (“Olah’s reagent”) to mitigate the safety concerns of anhydrous, gaseous HF. This solution is in equilibrium with gaseous HF, with no pyridine detected in the gas phase and provides a safer alternative to anhydrous HF [143,147]. Metal precursors used included a diethylcyclopentadienyl complex for magnesium, a silylamide for lithium and an alkylamide for zirconium. All processes resulted in saturation at 150 °C, with growth rates below 1 Å/cycle (Figure 12). All films, except  $\text{AlF}_3$  and  $\text{ZnF}_2$ , were crystalline. Generally, the films contained less than 2 at.% of oxygen impurities, as determined with XPS. Only  $\text{ZrF}_4$  contained some carbon impurities in addition to the oxygen. The films appeared somewhat fluorine deficient, however this is speculated to be a result of preferential fluorine sputtering during the XPS measurement [143,147]. The  $\text{AlF}_3$  deposition from TMA and HF showed an interesting etching reaction: above 250 °C the precursor pulses etched the  $\text{AlF}_3$  film [143,149]. This reaction has later been exploited in developing atomic layer etching processes [170–172]. The  $\text{AlF}_3$  process has been successfully utilized in protecting freestanding  $\text{LiCoO}_2/\text{MWCNT}$  (multi-walled carbon nanotube)/nanocellulose fibril electrodes, showing better protection at high potentials compared to the more common artificial SEI material  $\text{Al}_2\text{O}_3$  [173].

$\text{Li}_3\text{AlF}_6$  has been deposited using subcycles of  $\text{AlF}_3$  and  $\text{LiF}$  using TMA and HF-pyridine and  $\text{LiHMDS}$  and HF-pyridine as precursors [51]. One subcycle of  $\text{AlF}_3$  and one subcycle of  $\text{LiF}$  were used at 150 °C and monoclinic  $\text{Li}_3\text{AlF}_6$  was obtained with a growth rate of 0.9 Å/cycle [51,146]. The films had a Li:Al ratio of 2.7:1, as determined with ICP-MS and carbon, silicon and oxygen impurities were below the XPS detection limit. The films had an ionic conductivity of  $7.5 \times 10^{-6}$  S/cm at room temperature [146], which is similar to the first reports from the literature on thermally evaporated amorphous  $\text{Li}_3\text{AlF}_6$  films [12,13]. Interestingly, changing the pulsing ratio to three subcycles of  $\text{AlF}_3$  and one  $\text{LiF}$  resulted in the same metal ratio in the as-deposited film as the pulsing ratio of 1:1, suggesting a similar conversion reaction as we have seen in our experiments on  $\text{LiF}$  [151] and  $\text{Li}_3\text{AlF}_6$  [139].

## 5.2. ALD of Metal Fluorides Using Metal Fluorides as the Fluorine Source

The deposition of many metal fluorides has been studied at the University of Helsinki using  $\text{TiF}_4$  as the fluorine source, including materials such as  $\text{MgF}_2$ ,  $\text{LaF}_3$  and  $\text{CaF}_2$  [153,155,157,158].  $\text{TiF}_4$  is a relatively safe alternative to HF, since it is a solid at room temperature. It possesses relatively high volatility and thermal stability, combined with high reactivity, which are vital attributes for an effective ALD precursor. The use of  $\text{TiF}_4$  is made possible by a net ligand exchange reaction with a metal thd-complex (Equation (2)):



Other volatile side products, such as  $\text{TiF}_x(\text{thd})_{4-x}$  can form in addition. Recently this precursor was also demonstrated in an ALD process used in conjunction with  $\text{AlCl}_3$  [156].

Generally, metal fluorides deposited using  $\text{TiF}_4$  as the fluorine source show a decrease in growth rate as the deposition temperature is increased (Figure 12) [155]. This decrease has been proposed to be due to a decrease in the  $\text{TiF}_x$  adsorption density but this has not been verified experimentally. Using  $\text{TiF}_4$  as the fluorine source leads to higher growth rates compared to the use of HF, possibly due to the formation of the fluoride in question during both precursor pulses [155,156]. When using  $\text{TiF}_4$  as the fluorine source, the film growth usually shows saturation with respect to the fluorine precursor (Figure 13b) but the metal precursor can show either poor [150,153,157] or good saturation [158], depending on the material deposited (Figure 13a). Pilvi et al. postulated that the reason for

the non-saturative behaviour might be either slow kinetics or an enhancement of metal precursor decomposition caused by the  $\text{TiF}_x$ -surface groups [153]. Films deposited with  $\text{TiF}_4$  are generally very close to stoichiometric, as determined with ERDA (Figure 12d). Titanium is often found as an impurity in the deposited films but usually in only very small amounts [150,153,155]. Still, this impurity can limit the UV transmittance of these films when optical applications are the goal. The impurity level decreases as the deposition temperature is increased but at the same time film roughness increases resulting in more scattering of UV-light [153,157,158].

In an effort to obtain even purer metal fluoride films for optical applications, deposition of  $\text{MgF}_2$  has been studied using  $\text{TaF}_5$  as the fluorine source [154]. The growth process is very similar to that using  $\text{TiF}_4$  (Figure 12a) although with using  $\text{TaF}_5$  saturation with respect to the  $\text{Mg}(\text{thd})_2$  pulse length is observed. The films contained lower metal impurity levels than those deposited with  $\text{TiF}_4$  and in addition the films were much smoother at high deposition temperatures [153,154]. This low roughness resulted in improved optical properties.

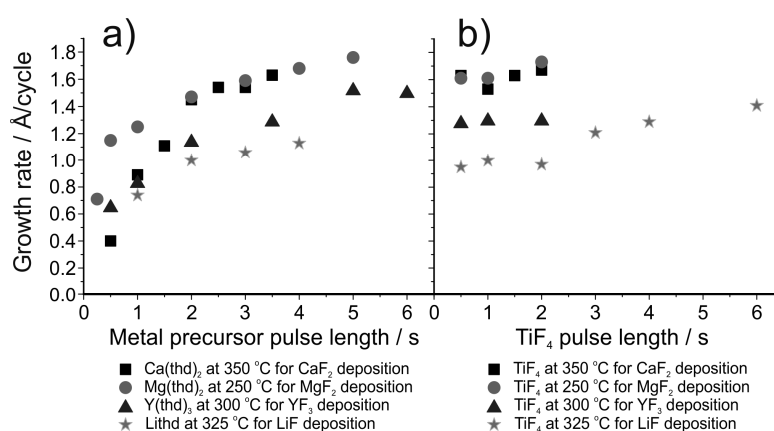


**Figure 13.** (a) Saturation curves for the metal precursor for  $\text{CaF}_2$ ,  $\text{MgF}_2$ ,  $\text{YF}_3$  and  $\text{LiF}$  deposition processes; (b) Saturation curves for the fluorine precursor  $\text{TiF}_4$  for  $\text{CaF}_2$ ,  $\text{MgF}_2$ ,  $\text{YF}_3$  and  $\text{LiF}$  processes. Data obtained from [150,153,155,157].

Following the work of Pilvi et al., a process for the deposition of  $\text{LiF}$  was developed [150].  $\text{LiThd}$  and  $\text{TiF}_4$  were used as precursors and the deposition temperature was varied between 250 and 350 °C. Crystalline  $\text{LiF}$  films with only small proportions of impurities were obtained at all deposition temperatures. Saturation of the growth was not found for  $\text{LiThd}$  at 325 °C (Figure 13a).  $\text{TiF}_4$ , on the other hand, showed saturation type behaviour between 0.5 and 2.0 s pulses. With longer pulse times, the growth rate increased linearly. Such an increase has not been observed with other processes utilizing  $\text{TiF}_4$ , however in these studies the  $\text{TiF}_4$  pulse lengths have been limited to 2 s or less (Figure 13b) [153,155,157,158].

The pulsing sequence  $\text{Mg}(\text{thd})_2 + \text{TiF}_4 + \text{LiThd} + \text{TiF}_4$  can produce  $\text{LiF}$  thin films between 300 and 350 °C [151]. Unlike the  $\text{LiThd} + \text{TiF}_4$  process of ref. [150], this sequence shows both an ALD window between 325 and 350 °C and saturation with respect to both  $\text{LiThd}$  and  $\text{TiF}_4$  (Figure 14). The growth rate at 325 °C was 1.4 Å/cycle, as opposed to 1.0 Å/cycle in the previous  $\text{LiF}$  process. All the films were again highly crystalline, with the film roughness being 19–20 nm for 70–80 nm films regardless of the deposition temperature. ToF-ERDA measurements showed the films to be very pure  $\text{LiF}$ , with only minute amounts of Mg and Ti impurities. C and H formed the largest part of impurities, however both were below 1 at.% in the deposition temperature range of 300–350 °C. It is surprising that despite the use of  $\text{Mg}(\text{thd})_2$  in the pulsing sequence, no magnesium ended up in the  $\text{LiF}$  films. We have proposed a mechanism to explain the deposition process (Equations (3)–(6)). In Equation (3),  $\text{Mg}(\text{thd})_2$  and  $\text{TiF}_4$  deposit  $\text{MgF}_2$  as has been previously reported [153]. In Equation (4),  $\text{Li}^+$  from  $\text{LiThd}$  replaces  $\text{Mg}^{2+}$  in the fluoride film and forms  $\text{LiF}$ . Magnesium leaves the films as  $\text{Mg}(\text{thd})_2$ , because the low levels of O,

C and H impurities imply that virtually no ligand decomposition is occurring during the growth. This type of fluoride-to- $\beta$ -diketonate ligand exchange might at first seem unexpected, however it has been reported that metal oxides can be dry etched using  $\beta$ -diketone vapours to form volatile  $\beta$ -diketonato complexes of metal ions [174]. After the removal of magnesium, Lithd adsorbs onto the formed lithium fluoride (Equation (5)) and is converted to LiF during the last  $\text{TiF}_4$  pulse (Equation (6)).

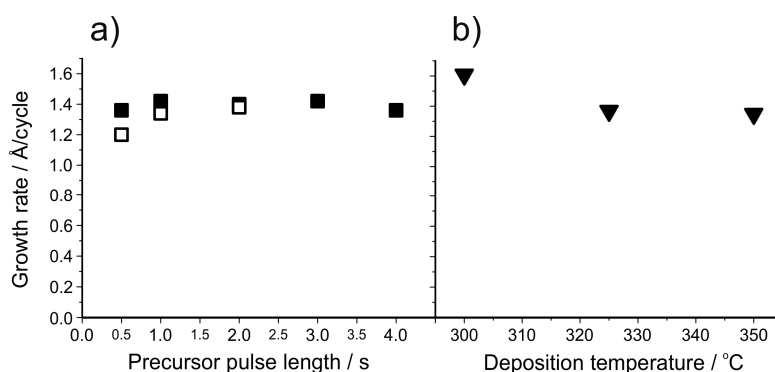
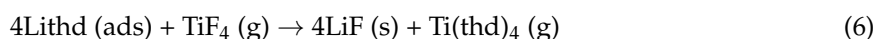
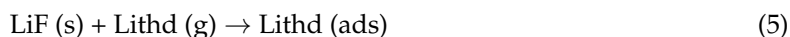
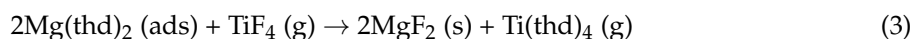


**Figure 14.** (a) Growth rate of LiF films as a function of Lithd (black squares) and  $\text{TiF}_4$  (white squares) pulse lengths at 325 °C; (b) Growth rate of LiF films as a function of deposition temperature. Data from [151].

Xie et al. have studied the use of  $\text{LiO}^t\text{Bu}$  instead of Lithd with  $\text{TiF}_4$  as the fluorine source [124]. This precursor combination led to the deposition of crystalline LiF between 200 and 300 °C. The maximum growth rate of 0.5 Å/cycle was achieved at 250 °C. The films had a refractive index close to 1.4 and a Li:F ratio of 1:0.97. Little else has been reported on the process thus far.

Similar to the methodology of using  $\text{TiF}_4$  or  $\text{TaF}_5$  as fluorine sources, Mane et al. have reported on the deposition of LiF using  $\text{LiO}^t\text{Bu}$  and either  $\text{WF}_6$  or  $\text{MoF}_6$  as the fluorine source [152]. Film growth took place between 150 and 300 °C, with amorphous films being deposited at the lowest temperature. This is an interesting finding, as using LiHMDS and HF-py at 150 °C led to crystalline LiF films [147]. With  $\text{MoF}_6$  as the fluorine source the films had a growth rate of 2.6 Å/cycle, which is much higher than that obtained with the Lithd +  $\text{TiF}_4$  process [150]. The films showed a 1:1 ratio of Li and F, with very small amounts of oxygen and carbon impurities. Most importantly, metal impurities were not detected with XPS.

After the success of alkaline and alkaline earth metal fluoride deposition, our group studied  $\text{Al}(\text{thd})_3$  and  $\text{TiF}_4$  as precursors for  $\text{AlF}_3$  [156]. However, this precursor combination led to no film growth on silicon and aluminum oxide. Our assumption is that this lack of reactivity has to do with the presence of aluminum-oxygen bonds in the  $\text{Al}(\text{thd})_3$  complex. Therefore, another aluminum precursor was needed in combination with  $\text{TiF}_4$ .  $\text{AlCl}_3$  is a widely used ALD precursor, with no oxygen present in the molecule. In addition,  $\text{TiCl}_4$  is a well-known, volatile ALD precursor [175,176], which is encouraging considering the expected ligand-exchange reaction taking place between  $\text{AlCl}_3$  and  $\text{TiF}_4$ . Thus, this combination was studied for the deposition of  $\text{AlF}_3$  [156]. Film growth was observed between 160 and 340 °C (Figure 12c). The saturation of the growth rate was studied at 160, 200 and 240 °C (Figure 15a).  $\text{TiF}_4$  showed similar behaviour as in the LiF case [150], with an increased

growth rate with the longest pulse times.  $\text{AlCl}_3$ , on the other hand, showed an opposite trend with growth rates decreasing as a function of pulse time.  $\text{AlCl}_3$  vapour has been reported to enhance the volatility of  $\text{AlF}_3$  [177], which might explain the etching-type behaviour seen in this process. As already mentioned, a similar decrease in the growth rate of  $\text{AlF}_3$  was also observed in the TMA + HF-py process. Despite these effects, the  $\text{AlF}_3$  growth rate remained constant with different cycle numbers at all temperatures studied (Figure 15b) [156]. ToF-ERDA measurements revealed that the films contained decreasing amounts of Cl and Ti impurities as the deposition temperature was increased, both being well below 1 at.% at 280 °C. However, the H and O impurities showed the opposite trend, with the films deposited at 280 °C containing up to 6 at% of oxygen.

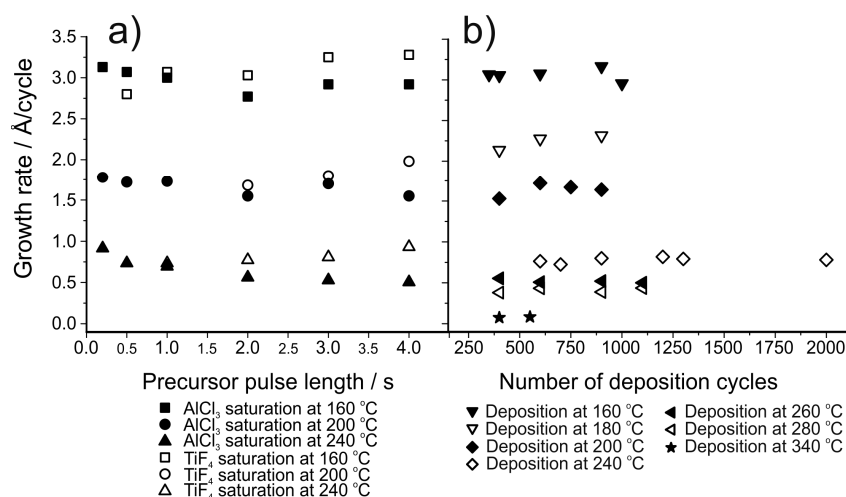


**Figure 15.** (a) Growth rate of  $\text{AlF}_3$  films as a function of  $\text{AlCl}_3$  (black) and  $\text{TiF}_4$  (white) pulse lengths at 160, 200 and 240 °C; (b) Growth rate of  $\text{AlF}_3$  films as a function of deposition cycles at various deposition temperatures. The  $\text{AlCl}_3$  pulse time was 0.5 s and the  $\text{TiF}_4$  pulse time was 1 s. Data from [156].

Jackson et al. have attempted to combine the methods discussed above for the deposition of  $\text{AlF}_3$  by using TMA and  $\text{TaF}_5$  as precursors [145]. This approach is somewhat questionable, as it has been reported that combining TMA with metal halides generally leads to metal carbide deposition [178–180]. In addition, a similar ligand exchange reaction between TMA and  $\text{TaF}_5$ , as was depicted in Equation (2), should produce pentamethyl tantalum which has been reported to be unstable [181,182]. Indeed, significant amounts of  $\text{TaC}_x$  were deposited at elevated temperatures [145]. At 125 °C the content of tantalum impurity was decreased and the process showed ALD-like behaviour. The films contained approximately 20 at.% of oxygen, meaning that the process is unable to deposit good quality  $\text{AlF}_3$ . Despite the large amounts of impurities, the deposition of this material onto a high-voltage lithium-ion battery cathode nickel-manganese-cobalt oxide (NMC) led to significant improvements in its rate performance (Figure 16).

Similar to Jackson et al., Park et al. used TMA with  $\text{WF}_6$  to deposit an amorphous composite fluoride composed of  $\text{AlF}_3$  and metallic W and  $\text{WC}_x$  [144,159]. The material was studied as an artificial SEI layer for  $\text{LiCoO}_2$  cathodes and was found to improve the cycling properties of the material. It appeared that the composite nature increased the electron conductivity of the fluoride layer while still retaining its chemical inertness.

Our group has also studied ternary fluoride deposition using metal fluorides as precursors [139]. The deposition of  $\text{Li}_3\text{AlF}_6$  proved complicated when using the binary processes of  $\text{LiF}$  and  $\text{AlF}_3$  described in Refs. [150,151,156]: uncontrollable conversion of  $\text{AlF}_3$  to  $\text{LiF}$  by Lithd was a threat to using the ALD subcycle approach. More importantly, exposing  $\text{LiF}$  to  $\text{AlCl}_3$  could result in undesirable  $\text{LiCl}$  formation. Thus, attempts at depositing  $\text{Li}_3\text{AlF}_6$  were made using two processes (Figure 17) [139]. In Process 1,  $\text{Al}(\text{thd})_3$  and  $\text{TiF}_4$  were pulsed sequentially onto  $\text{LiF}$  thin films and a conversion reaction

to the ternary  $\text{Li}_3\text{AlF}_6$  took place during the deposition process. In Process 2,  $\text{AlF}_3$  films were exposed to Lithd vapour in an ALD reactor (described in more detail in section “5.3. Other Approaches to ALD of Metal Fluorides”). In Process 1,  $\text{Al}(\text{thd})_3$  was used instead of  $\text{AlCl}_3$  to avoid  $\text{Li}^+$  contact with  $\text{Cl}^-$  from  $\text{AlCl}_3$ . Despite the prior knowledge that  $\text{Al}(\text{thd})_3$  and  $\text{TiF}_4$  do not produce  $\text{AlF}_3$  on silicon substrates [156], a reaction did occur between these precursors when pulsed onto LiF films. The fluorides mixed together during the deposition process, resulting in crystalline  $\text{Li}_3\text{AlF}_6$  with crystalline LiF residues. High deposition temperatures together with long  $\text{Al}(\text{thd})_3$  pulses resulted in less LiF impurity in the film, as observed with GIXRD. However, these same conditions worsened the visual appearance of the films. ToF-ERDA revealed that even in the best samples, the content of Al was very low, although  $\text{Li}_3\text{AlF}_6$  was clearly visible in the X-ray diffractograms. In addition, the level of titanium impurity was high. Thus, it was concluded that in the end Process 1 was not efficient in depositing  $\text{Li}_3\text{AlF}_6$ .

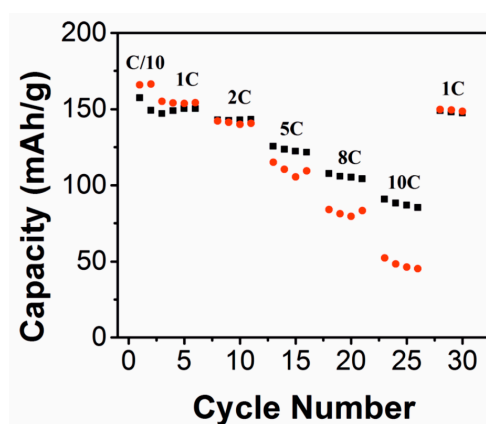


**Figure 16.** Gravimetric capacity of coin cells as a function of cycle number with different discharge rates. Black squares denote an NMC-cathode coated with TMA +  $\text{TaF}_5$ . Red circles denote uncoated NMC. Reprinted with permission from [145]. Copyright 2016 American Vacuum Society.

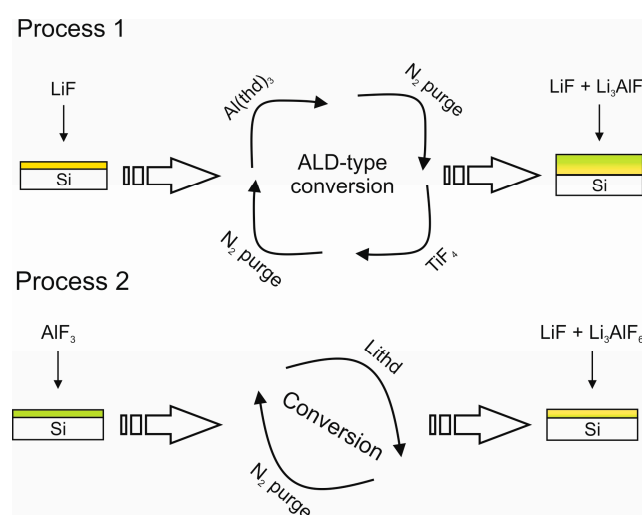


**Figure 17.** Process 1 utilizes  $\text{Al}(\text{thd})_3$  and  $\text{TiF}_4$  in a conversion reaction to form  $\text{Li}_3\text{AlF}_6$  out of LiF thin films. Process 2 uses a conversion reaction between ALD-made  $\text{AlF}_3$  and the lithium precursor Lithd to deposit  $\text{Li}_3\text{AlF}_6$ . Reprinted with permission from [139]. Copyright 2017 Elsevier.

Recently, Xie et al. published their results on the deposition of  $\text{LiAlF}_4$  [124]. By combining the processes for LiF and  $\text{AlF}_3$  using  $\text{LiO}^t\text{Bu}$ ,  $\text{AlCl}_3$  and  $\text{TiF}_4$  as precursors they were able to deposit

amorphous  $\text{LiAlF}_4$  with a Li:Al ratio of 1.2:1 and an ionic conductivity of  $3.5 \times 10^{-8}$  S/cm. The  $\text{LiAlF}_4$  film was used as a protective layer on top of a lithium nickel manganese cobalt oxide cathode and was found to improve the stability of the cathode without sacrificing its rate performance.

### 5.3. Other Approaches to ALD of Metal Fluorides

Putkonen et al. provided other interesting pathways for avoiding the use of HF in fluoride deposition by depositing metal fluorides through oxide chemistry [160]. They found that by using the fluorinated  $\beta$ -diketonate precursor  $\text{Ca}(\text{hfac})_2$  and ozone as precursors  $\text{CaF}_2$  is deposited, instead of  $\text{CaCO}_3$  that is formed when the non-fluorinated  $\beta$ -diketonate  $\text{Ca}(\text{thd})_2$  is used together with ozone [183]. The fluoride films had a growth rate of  $0.3 \text{ \AA}/\text{cycle}$  at  $300 \text{ }^\circ\text{C}$  and were close to stoichiometric, although approximately 5 at.% of oxygen was present in the films [160]. An even more interesting approach to  $\text{CaF}_2$  used the non-fluorinated metal precursor  $\text{Ca}(\text{thd})_2$  in combination with ozone and the  $\text{Hhfac}$  molecule. First,  $\text{Ca}(\text{thd})_2$  was pulsed onto the substrate followed by an ozone pulse, resulting in  $\text{CaCO}_3$  deposition. Then  $\text{Hhfac}$ , which is known to adsorb to surfaces, was pulsed followed again by an ozone pulse. Ozone breaks down the  $\text{Hhfac}$  on the surface, providing fluoride ions which react with the calcium ions, resulting in a conversion reaction from  $\text{CaCO}_3$  to  $\text{CaF}_2$ . This process provided a growth rate of  $0.4 \text{ \AA}/\text{cycle}$  between  $250$  and  $350 \text{ }^\circ\text{C}$ , which is close to the rate of  $\text{CaCO}_3$  deposition from  $\text{Ca}(\text{thd})_2$  and ozone in similar conditions. The  $\text{CaF}_2$  films were polycrystalline and close to stoichiometric and the amount of oxygen was below the detection limit of Rutherford backscattering spectroscopy (RBS). The same approach was reported to be successful also for  $\text{MgF}_2$  and  $\text{LaF}_3$  deposition.

Vos et al. recently reported on an interesting process for depositing  $\text{AlF}_3$  using TMA and  $\text{SF}_6$  plasma [161]. Plasma-enhanced ALD processes have not been previously available for fluoride deposition. However, F-containing plasmas, such as  $\text{CF}_4$ , have been widely used for etching processes. In this work,  $\text{SF}_6$  was used because it is stable and non-toxic. Inductively coupled  $\text{SF}_6$  plasmas contain species such as  $\text{F}$ ,  $\text{F}_2$ ,  $\text{SF}_5^+$  and  $\text{F}^-$  with S and  $\text{S}^+$  as minor components. The  $\text{AlF}_3$  deposition showed saturation with both TMA and the plasma with good film uniformity and conformality. As with all other  $\text{AlF}_3$  processes, the film growth rate decreased with increasing deposition temperature, being  $0.85 \text{ \AA}/\text{cycle}$  at  $200 \text{ }^\circ\text{C}$ . All the films were amorphous with very low S and O impurity levels and an Al:F ratio close to stoichiometric.

After noting that the pulsing sequence  $\text{Mg}(\text{thd})_2 + \text{TiF}_4 + \text{Lithd} + \text{TiF}_4$  produced LiF with little to no Mg impurities, our group studied the conversion reaction of  $\text{MgF}_2$  films upon exposure to Lithd [151]. As it turned out, with high enough Lithd doses  $\text{MgF}_2$  films of 150 nm in thickness could be converted into LiF with no indication of  $\text{MgF}_2$  or Mg impurities in GIXRD, EDX or ToF-ERDA measurements. The lower the reaction temperature, the larger the Lithd dose needed to completely convert the  $\text{MgF}_2$  film into LiF. Although the resulting LiF films were again highly crystalline as determined with GIXRD, they showed much smaller grain sizes and thus lower roughness than the films deposited with either the two [150] or four [151] step LiF processes (Figure 18). In addition, the adhesion of the films to the silicon substrates was markedly improved. Our experiments demonstrated that the conversion reaction with Lithd is not limited to the surface regions of  $\text{MgF}_2$  films but can in fact proceed very deeply into the films. The high mobility and reactivity of  $\text{Li}^+$  seen in these experiments is likely to play a role in many processes used to deposit materials containing lithium, especially in the case of ternaries. For example, Miikkulainen et al. later reported similar results in their conversion experiments to form spinel  $\text{LiMn}_2\text{O}_4$  using  $\text{MnO}_2$  films and Lithd, as was already discussed in a previous section [90]. However, their conversion reaction also led to significant amounts of hydrogen and carbon impurities when no ozone was used after the Lithd pulse, as opposed to our conversion reactions of  $\text{MgF}_2$  with Lithd which led to purer film products.

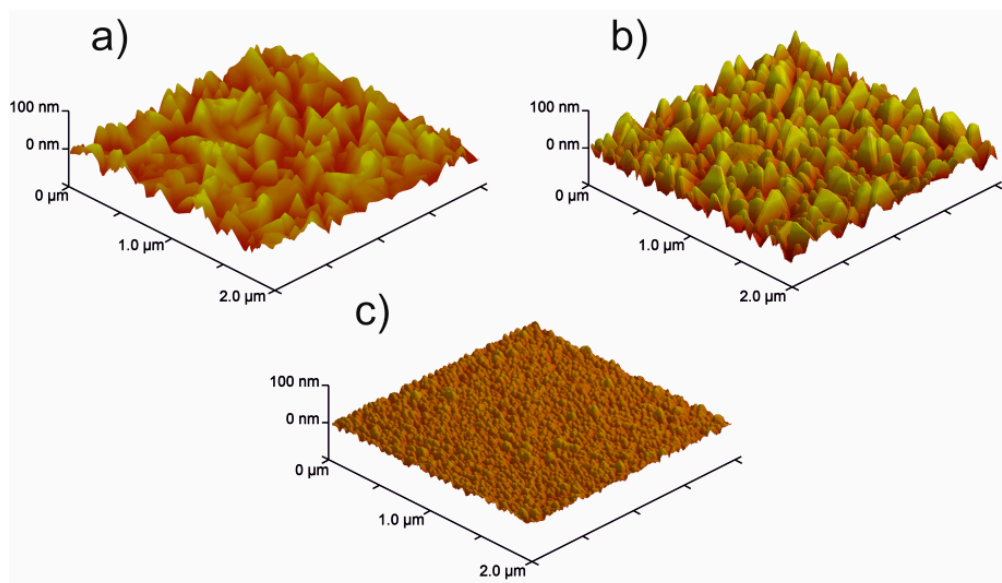


**Figure 18.** AFM images of LiF films deposited at 325 °C using three different processes: (a) Lithd + TiF<sub>4</sub>, thickness 73 nm, rms roughness 15.9 nm; (b) Mg(thd)<sub>2</sub> + TiF<sub>4</sub> + Lithd + TiF<sub>4</sub>, thickness 68 nm, rms roughness 20.1 nm; (c) conversion from a MgF<sub>2</sub> film using Lithd, thickness 94 nm, rms roughness 4.8 nm.

Li<sub>3</sub>AlF<sub>6</sub> was also deposited using a similar conversion reaction as with MgF<sub>2</sub> and Lithd (Process 2, Figure 17) [139]. Approximately 50 and 100 nm thin films of AlF<sub>3</sub> were exposed to the lithium precursor at different temperatures and for different Lithd pulse numbers to determine whether good quality Li<sub>3</sub>AlF<sub>6</sub> could form from this conversion reaction. GIXRD analyses showed that amorphous AlF<sub>3</sub> transformed into monoclinic Li<sub>3</sub>AlF<sub>6</sub> with Lithd exposure. Choosing too large a number of Lithd pulses resulted in crystalline LiF formation. The mechanism of the conversion is most likely similar to the MgF<sub>2</sub> conversion, as the oxygen, carbon and hydrogen impurity levels were very low in the films after the conversion, as determined with ToF-ERDA. Despite crystalline Li<sub>3</sub>AlF<sub>6</sub> being visible in the X-ray diffractograms, obtaining the correct Li:Al ratio was challenging. ToF-ERDA revealed that doubling the Lithd exposure from 20 to 40 pulses increased the Li:Al ratio from 0.93:1 to 7.9:1 for approx. 50 nm AlF<sub>3</sub> films (Figure 19). With 100 nm AlF<sub>3</sub> films exposed to 40 Lithd pulses, the ratio varied between 1.33:1 and 1.49:1. Thus, thinner films were much faster to convert than thicker ones, as was to be expected. The exposure temperature also played a role in the conversion. Just a 25 °C increase from 250 to 275 °C increased the Li:Al ratio for a 40 pulse sample from 1.49:1 to 2:1. However, despite the lithium deficient metal ratio, the 275 °C exposure temperature sample already contained a prominent amount of crystalline LiF based on GIXRD. The converted films showed a porous structure in FESEM (field emission scanning electron microscopy) (Figure 20), preventing ionic conductivity measurements due to top electrodes short circuiting with the bottom electrode.

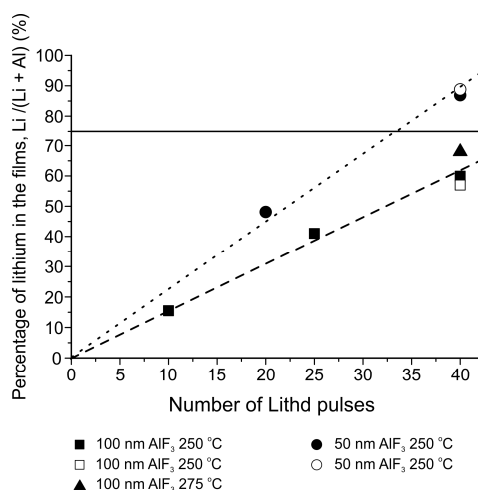


**Figure 19.** The content of lithium cations in converted  $\text{AlF}_3$  films as a function of the number of Lithd pulses. Black and white symbols denote samples prepared at different times but with same exposure parameters. Dotted and dashed lines illustrate that the content of lithium increases linearly with the number of Lithd pulses. The solid line illustrates the correct metal stoichiometry of  $\text{Li}_3\text{AlF}_6$ . Data from [139].

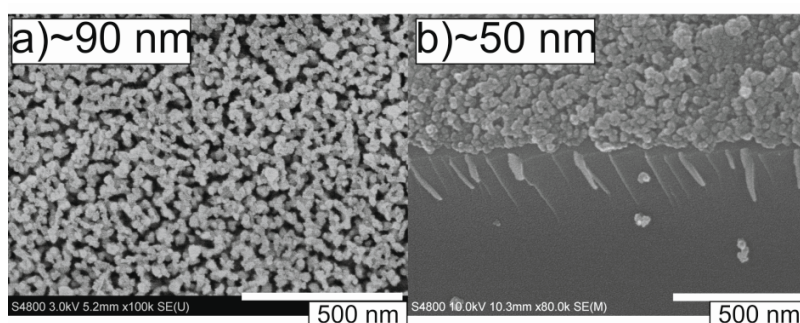


**Figure 20.** FESEM images of (a) ~90 nm crystalline  $\text{Li}_3\text{AlF}_6$  film made by conversion from  $\text{AlF}_3$  and Lithd and (b) ~50 nm crystalline  $\text{Li}_3\text{AlF}_6$  film made by conversion from  $\text{AlF}_3$  and Lithd and taken by tilting the sample.

## 6. Conclusions

Metal fluorides could provide an interesting, high voltage and high capacity alternative to current oxide based lithium-ion battery cathode materials. However, because most metal fluorides act as conversion cathodes, special effort must be made to enhance their cycling ability and to alleviate problems related to electrode pulverization. For some fluorides, encouraging lithium-ion conductivities have been measured, meaning that they could act as highly stable solid electrolytes in all-solid-state Li-ion batteries. In addition, fluoride thin films have been shown to function as artificial solid-electrolyte-interface layers, protecting both cathodes and anodes from metal dissolution and other undesired side reactions during battery cycling. All these results show that there is a lot of untapped potential in this class of battery materials, worthy of more research. For future applications, methods producing high quality, conformal fluoride thin films with precise thickness control are needed, for example for depositing cathodes in intricate 3D structures and for depositing protecting films of 1 nm or less on current electrode materials. Atomic layer deposition can be the method for answering these demands. The lithium-ion exhibits unique ALD chemistries through its high mobility, which needs to be taken into account when designing processes for battery material deposition by ALD.

Many metal fluoride thin films have been deposited using ALD, however the focus of these studies has mainly been on optical applications. Only very recently studies on the deposition of materials such as  $\text{AlF}_3$  and  $\text{Li}_3\text{AlF}_6$  have emerged, with the main motivation of utilizing these materials in lithium-ion batteries. In the future, much more research effort should be put into depositing transition metal fluorides and multi-component fluorides for use in lithium-ion batteries. These materials have received next to no interest in the past 25 years of ALD fluoride studies, meaning there is much to be discovered in this area of materials science. These future studies will undoubtedly greatly benefit from recent studies utilizing new fluorine sources such as metal fluorides and  $\text{SF}_6$  plasma.

**Author Contributions:** Writing—Original Draft Preparation, M.M.; Writing—Review & Editing, M.M.; M.R.; M.L.; Visualization, M.M.; Supervision, M.R.; M.L.

**Funding:** This work was funded by the Finnish Centre of Excellence in Atomic Layer Deposition (284623).

**Acknowledgments:** Peter J. King is thanked for proof-reading this work.

**Conflicts of Interest:** The authors declare no conflict of interest.

## References

1. Tesla Solar Roof. Available online: <https://www.tesla.com/solarroof> (accessed on 12 May 2018).
2. Pillot, C. The worldwide battery market 2011–2025. In Proceedings of the Batteries 2012, Nice, France, 24–26 October 2012.
3. Batteries storing power seen as big as rooftop solar in 12 years. Available online: <https://www.bloomberg.com/news/articles/2016-06-13/batteries-storing-power-seen-as-big-as-rooftop-solar-in-12-years> (accessed on 12 May 2018).
4. Oudenhoven, J.F.M.; Baggetto, L.; Notten, P.H.L. All-solid-state lithium-ion microbatteries: A review of various three-dimensional concepts. *Adv. Energy Mater.* **2011**, *1*, 10–33. [[CrossRef](#)]
5. Hayner, C.M.; Zhao, X.; Kung, H.H. Materials for Rechargeable Lithium-Ion Batteries. *Annu. Rev. Chem. Biomol. Eng.* **2012**, *3*, 445–471. [[CrossRef](#)] [[PubMed](#)]
6. Knoop, H.C.M.; Donders, M.E.; van de Sanden, M.C.M.; Notten, P.H.L.; Kessels, W.M.M. Atomic layer deposition for nanostructured Li-ion batteries. *J. Vac. Sci. Technol. A* **2012**, *30*, 010801. [[CrossRef](#)]
7. Marichy, C.; Bechelany, M.; Pinna, N. Atomic Layer Deposition of Nanostructured Materials for Energy and Environmental Applications. *Adv. Mater.* **2012**, *24*, 1017–1032. [[CrossRef](#)] [[PubMed](#)]
8. Long, J.W.; Dunn, B.; Rolison, D.R.; White, H.S. Three-Dimensional Battery Architectures. *Chem. Rev.* **2004**, *104*, 4463–4492. [[CrossRef](#)] [[PubMed](#)]
9. Nitta, N.; Yushin, G. High-capacity anode materials for lithium-ion batteries: Choice of elements and structures for active particles. *Part. Part. Syst. Character.* **2014**, *31*, 317–336. [[CrossRef](#)]
10. Zhu, C.; Han, K.; Geng, D.; Ye, H.; Meng, X. Achieving high-performance silicon anodes of lithium-ion batteries via atomic and molecular layer deposited surface coatings: An overview. *Electrochim. Acta* **2017**, *251*, 710–728. [[CrossRef](#)]
11. Amatucci, G.G.; Pereira, N. Fluoride based electrode materials for advanced energy storage devices. *J. Fluor. Chem.* **2007**, *128*, 243–262. [[CrossRef](#)]
12. Oi, T. Ionic conductivity of amorphous  $\text{mLiFnMF}_3$  thin films ( $M = \text{Al, Cr, Sc or Al + Sc}$ ). *Mat. Res. Bull.* **1984**, *19*, 1343–1348. [[CrossRef](#)]
13. Oi, T. Ionic conductivity of  $\text{LiF}$  thin films containing Di- or trivalent metal fluorides. *Mat. Res. Bull.* **1984**, *19*, 451–457. [[CrossRef](#)]
14. Oi, T. Ionic conductivity of amorphous ternary fluoride thin films of composition  $\text{Li}_2\text{M}^{\text{II}}\text{M}^{\text{III}}\text{F}_7$  ( $\text{M}^{\text{II}} = \text{Mg, Fe; M}^{\text{III}} = \text{Al, Sc}$ ). *Mat. Res. Bull.* **1984**, *19*, 1077–1082. [[CrossRef](#)]
15. Huggins, R.A. *Advanced Batteries: Materials Science Aspects*; Springer: New York, NY, USA, 2009; ISBN 978-0-387-76424-5.
16. Tarascon, J.-M.; Armand, M. Issues and challenges facing rechargeable lithium batteries. *Nature* **2001**, *414*, 359–367. [[CrossRef](#)] [[PubMed](#)]
17. Baggetto, L.; Niessen, R.A.H.; Roozeboom, F.; Notten, P.H.L. High energy density all-solid-state batteries: A challenging concept towards 3D integration. *Adv. Funct. Mater.* **2008**, *18*, 1057–1066. [[CrossRef](#)]

18. Whittingham, M.S. Lithium batteries and cathode materials. *Chem. Rev.* **2004**, *104*, 4271–4302. [[CrossRef](#)] [[PubMed](#)]
19. Ellis, B.L.; Lee, K.T.; Nazar, L.F. Positive electrode materials for Li-Ion and Li-batteries. *Chem. Mater.* **2010**, *22*, 691–714. [[CrossRef](#)]
20. Chen, Z.; Qin, Y.; Amine, K.; Sun, Y.-K. Role of surface coating on cathode materials for lithium-ion batteries. *J. Mater. Chem.* **2010**, *20*, 7606–7612. [[CrossRef](#)]
21. Park, J.S.; Meng, X.; Elam, J.W.; Hao, S.; Wolverton, C.; Kim, C.; Cabana, J. Ultrathin lithium-ion conducting coatings for increased interfacial stability in high voltage lithium-ion batteries. *Chem. Mater.* **2014**, *26*, 3128–3134. [[CrossRef](#)]
22. Guan, D.; Jeevarajan, J.A.; Wang, Y. Enhanced cycleability of  $\text{LiMn}_2\text{O}_4$  cathodes by atomic layer deposition of nanosized-thin  $\text{Al}_2\text{O}_3$  coatings. *Nanoscale* **2011**, *3*, 1465–1469. [[CrossRef](#)] [[PubMed](#)]
23. Jung, Y.S.; Cavanagh, A.S.; Riley, L.A.; Kang, S.-H.; Dillon, A.C.; Groner, M.D.; George, S.M.; Lee, S.-H. Ultrathin direct atomic layer deposition on composite electrodes for highly durable and safe Li-Ion batteries. *Adv. Mater.* **2010**, *22*, 2172–2176. [[CrossRef](#)] [[PubMed](#)]
24. Jung, Y.S.; Cavanagh, A.S.; Dillon, A.C.; Groner, M.D.; George, S.M.; Lee, S.-H. Enhanced stability of  $\text{LiCoO}_2$  cathodes in lithium-ion batteries using surface modification by atomic layer deposition. *J. Electrochem. Soc.* **2010**, *157*, A75–A81. [[CrossRef](#)]
25. Nitta, N.; Wu, F.; Lee, J.T.; Yushin, G. Li-ion battery materials: Present and future. *Mater. Today* **2015**, *18*, 252–264. [[CrossRef](#)]
26. Xu, W.; Wang, J.; Ding, F.; Chen, X.; Nasybulin, E.; Zhang, Y.; Zhang, J.-G. Lithium metal anodes for rechargeable batteries. *Energy Environ. Sci.* **2014**, *7*, 513–537. [[CrossRef](#)]
27. Poizot, P.; Laruelle, S.; Grugeon, S.; Dupont, L.; Tarascon, J.-M. Nano-sized transition-metal oxides as negative-electrode materials for lithium-ion batteries. *Nature* **2000**, *407*, 496–499. [[CrossRef](#)] [[PubMed](#)]
28. Park, C.-M.; Kim, J.-H.; Kim, H.; Sohn, H.-J. Li-alloy based anode materials for Li secondary batteries. *Chem. Soc. Rev.* **2010**, *39*, 3115–3141. [[CrossRef](#)] [[PubMed](#)]
29. Li, H.; Balaya, P.; Maier, J. Li-Storage via heterogeneous reaction in selected binary metal fluorides and oxides. *J. Electrochem. Soc.* **2004**, *151*, A1878–A1885. [[CrossRef](#)]
30. Thangadurai, V.; Weppner, W. Solid state lithium ion conductors: Design considerations by thermodynamic approach. *Ionics* **2002**, *8*, 281–292. [[CrossRef](#)]
31. Thangadurai, V.; Weppner, W. Recent progress in solid oxide and lithium ion conducting electrolytes research. *Ionics* **2006**, *12*, 81–92. [[CrossRef](#)]
32. Xia, H.; Wang, H.L.; Xiao, W.; Lai, M.O.; Lu, L. Thin film Li electrolytes for all-solid-state micro-batteries. *Int. J. Surf. Sci. Eng.* **2009**, *3*, 23–43. [[CrossRef](#)]
33. Knauth, P. Inorganic solid Li ion conductors: An overview. *Solid State Ion.* **2009**, *180*, 911–916. [[CrossRef](#)]
34. Fergus, J.W. Ceramic and polymeric solid electrolytes for lithium-ion batteries. *J. Power Sources* **2010**, *195*, 4554–4569. [[CrossRef](#)]
35. Hu, M.; Pang, X.; Zhou, Z. Recent progress in high-voltage lithium ion batteries. *J. Power Sources* **2013**, *237*, 229–242. [[CrossRef](#)]
36. Cabana, J.; Monconduit, L.; Larcher, D.; Palacín, M.R. Beyond intercalation-based Li-ion batteries: The state of the art and challenges of electrode materials reacting through conversion reactions. *Adv. Mater.* **2010**, *22*, E170–E192. [[CrossRef](#)] [[PubMed](#)]
37. Li, H.; Richter, G.; Maier, J. Reversible formation and decomposition of  $\text{LiF}$  clusters using transition metal fluorides as precursors and their application in rechargeable Li batteries. *Adv. Mater.* **2003**, *15*, 736–739. [[CrossRef](#)]
38. Badway, F.; Cosandey, F.; Pereira, N.; Amatucci, G.G. Carbon metal fluoride nanocomposites: High-capacity reversible metal fluoride conversion materials as rechargeable positive electrodes for Li batteries. *J. Electrochem. Soc.* **2003**, *150*, A1318–A1327. [[CrossRef](#)]
39. Zhang, H.; Zhou, Y.-N.; Sun, Q.; Fu, Z.-W. Nanostructured nickel fluoride thin film as a new Li storage material. *Solid State Sci.* **2008**, *10*, 1166–1172. [[CrossRef](#)]
40. Bervas, M.; Badway, F.; Klein, L.C.; Amatucci, G.G. Bismuth fluoride nanocomposite as a positive electrode material for rechargeable lithium batteries. *Electrochem. Solid-State Lett.* **2005**, *8*, A179–A183. [[CrossRef](#)]
41. Gonzalo, E.; Kuhn, A.; García-Alvarado, F. On the room temperature synthesis of monoclinic  $\text{Li}_3\text{FeF}_6$ : A new cathode material for rechargeable lithium batteries. *J. Power Sources* **2010**, *195*, 4990–4996. [[CrossRef](#)]

42. Basa, A.; Gonzalo, E.; Kuhn, A.; García-Alvarado, F. Reaching the full capacity of the electrode material  $\text{Li}_3\text{FeF}_6$  by decreasing the particle size to nanoscale. *J. Power Sources* **2012**, *197*, 260–266. [[CrossRef](#)]
43. Basa, A.; Gonzalo, E.; Kuhn, A.; García-Alvarado, F. Facile synthesis of  $\beta\text{-Li}_3\text{VF}_6$ : A new electrochemically active lithium insertion material. *J. Power Sources* **2012**, *207*, 160–165. [[CrossRef](#)]
44. Koyama, Y.; Tanaka, I.; Adachi, H. New fluoride cathodes for rechargeable lithium batteries. *J. Electrochem. Soc.* **2000**, *147*, 3633–3636. [[CrossRef](#)]
45. Amalraj, F.; Talianker, M.; Markovsky, B.; Burlaka, L.; Leifer, N.; Goobes, G.; Erickson, E.M.; Haik, O.; Grinblat, J.; Zinigrad, E.; et al. Studies of Li and Mn-rich  $\text{Li}_x[\text{MnNiCo}]\text{O}_2$  electrodes: electrochemical performance, structure, and the effect of the aluminum fluoride coating. *J. Electrochem. Soc.* **2013**, *160*, A2220–A2233. [[CrossRef](#)]
46. Lee, S.-H.; Yoon, C.S.; Amine, K.; Sun, Y.-K. Improvement of long-term cycling performance of  $\text{Li}[\text{Ni}_{0.8}\text{Co}_{0.15}\text{Al}_{0.05}]\text{O}_2$  by  $\text{AlF}_3$  coating. *J. Power Sources* **2013**, *234*, 201–207. [[CrossRef](#)]
47. Sun, Y.-K.; Lee, M.-J.; Yoon, C.S.; Hassoun, J.; Amine, K.; Scrosati, B. The role of  $\text{AlF}_3$  coatings in improving electrochemical cycling of Li-enriched nickel-manganese oxide electrodes for Li-ion batteries. *Adv. Mater.* **2012**, *24*, 1192–1196. [[CrossRef](#)] [[PubMed](#)]
48. Tron, A.; Park, Y.D.; Mun, J.  $\text{AlF}_3$ -coated  $\text{LiMn}_2\text{O}_4$  as cathode material for aqueous rechargeable lithium battery with improved cycling stability. *J. Power Sources* **2016**, *325*, 360–364. [[CrossRef](#)]
49. Sun, Y.-K.; Cho, S.-W.; Myung, S.-T.; Amine, K.; Prakash, J. Effect of  $\text{AlF}_3$  coating amount on high voltage cycling performance of  $\text{LiCoO}_2$ . *Electrochim. Acta* **2007**, *53*, 1013–1019. [[CrossRef](#)]
50. Ding, F.; Xu, W.; Choi, D.; Wang, W.; Li, X.; Engelhard, M.H.; Chen, X.; Yang, Z.; Zhang, J.-G. Enhanced performance of graphite anode materials by  $\text{AlF}_3$  coating for lithium-ion batteries. *J. Mater. Chem.* **2012**, *22*, 12745–12751. [[CrossRef](#)]
51. Lee, Y.; Piper, D.M.; Cavanagh, A.S.; Young, M.J.; Lee, S.-H.; George, S.M. Atomic layer deposition of lithium ion conducting  $(\text{AlF}_3)(\text{LiF})_x$  alloys using trimethylaluminum, lithium hexamethyldisilazide and hydrogen fluoride-pyridine. In Proceedings of the 14th International Conference on Atomic Layer Deposition, Kyoto, Japan, 15–18 June 2014.
52. Miyazaki, R.; Maekawa, H.  $\text{Li}^+$ -ion conduction of  $\text{Li}_3\text{AlF}_6$  mechanically milled with  $\text{LiCl}$ . *ECS Electrochem. Lett.* **2012**, *1*, A87–A89. [[CrossRef](#)]
53. Dance, J.-M.; Oi, T. Ionic conductivity of amorphous lithium fluoride-nickel fluoride ( $m\text{LiF}-n\text{NiF}_2$ ) thin films. *Thin Solid Films* **1983**, *104*, L71–L73.
54. Kawamoto, Y.; Fujiwara, J.; Ichimura, C. Ionic conduction in  $x\text{MF}\cdot(95-x)\text{ZrF}_4\cdot 5\text{LaF}_3$  (M: Alkali metals) glasses: I. Lithium ion conduction in  $x\text{LiF}\cdot(95-x)\text{ZrF}_4\cdot 5\text{LaF}_3$  glasses. *J. Non-Cryst. Solids* **1989**, *111*, 245–251. [[CrossRef](#)]
55. Reau, J.M.; Kahnt, H.; Poulain, M. Ionic transport studies in mixed alkali-fluorine conductor glasses of composition  $\text{ZrF}_4\text{-BaF}_2\text{-LaF}_3\text{-AF}$  (A = Li, Na) and  $\text{ZrF}_4\text{-BaF}_2\text{-ThF}_4\text{-LiF}$ . *J. Non-Cryst. Solids* **1990**, *119*, 347–350. [[CrossRef](#)]
56. Senegas, J.; Reau, J.M.; Aomi, H.; Hagenmuller, P.; Poulain, M. Ionic conductivity and NMR investigation of quaternary glasses in the  $\text{ZrF}_4\text{-BaF}_2\text{-ThF}_4\text{-LiF}$  system. *J. Non-Cryst. Solids* **1986**, *85*, 315–334. [[CrossRef](#)]
57. Trnovcová, V.; Fedorov, P.P.; Bárta, Č.; Labaš, V.; Meleshina, V.A.; Sobolev, B.P. Microstructure and physical properties of superionic eutectic composites of the  $\text{LiF-RF}_3$  (R = rare earth element) system. *Solid State Ion.* **1999**, *119*, 173–180. [[CrossRef](#)]
58. Trnovcová, V.; Fedorov, P.P.; Furár, I. Fluoride solid electrolytes containing rare earth elements. *J. Rare Earths* **2008**, *26*, 225–232. [[CrossRef](#)]
59. Dieudonné, B.; Chable, J.; Mauvy, F.; Fourcade, S.; Durand, E.; Lebraud, E.; Leblanc, M.; Legein, C.; Body, M.; Maisonneuve, V.; et al. Exploring the  $\text{Sm}_{1-x}\text{Ca}_x\text{F}_{3-x}$  tysonite solid solution as a solid-state electrolyte: Relationships between structural features and  $\text{F}^-$  ionic conductivity. *J. Phys. Chem. C* **2015**, *119*, 25170–25179. [[CrossRef](#)]
60. Sorokin, N.I.; Sobolev, B.P. Nonstoichiometric fluorides-solid electrolytes for electrochemical devices: A review. *Crystallogr. Rep.* **2007**, *52*, 842–863. [[CrossRef](#)]
61. Reddy, M.A.; Fichtner, M. Batteries based on fluoride shuttle. *J. Mater. Chem.* **2011**, *21*, 17059–17062. [[CrossRef](#)]
62. Leskelä, M.; Ritala, M. Atomic layer deposition chemistry: Recent developments and future challenge. *Angew. Chem. Int. Ed.* **2003**, *42*, 5548–5554. [[CrossRef](#)] [[PubMed](#)]

63. George, S.M. Atomic layer deposition: An overview. *Chem. Rev.* **2010**, *110*, 111–131. [[CrossRef](#)] [[PubMed](#)]
64. Ritala, M.; Leskelä, M. Atomic layer deposition. In *Handbook of Thin Film Materials*; Nalwa, H.S., Ed.; Academic Press: San Diego, CA, USA, 2002; Volume 1, pp. 103–159. ISBN 9780125129084.
65. Profijt, H.B.; Potts, S.E.; van de Sanden, M.C.M.; Kessels, W.M.M. Plasma-assisted atomic layer deposition: Basics, opportunities, and challenges. *J. Vac. Sci. Technol. A* **2011**, *29*, 050801. [[CrossRef](#)]
66. Chalker, P.R. Photochemical atomic layer deposition and etching. *Surf. Coat. Technol.* **2016**, *291*, 258–263. [[CrossRef](#)]
67. Miikkulainen, V.; Väyrynen, K.; Kilpi, V.; Han, Z.; Vehkamäki, M.; Mizohata, K.; Räisänen, J.; Ritala, M. Photo-assisted ALD: Process development and application perspectives. *ECS Trans.* **2017**, *80*, 49–60. [[CrossRef](#)]
68. Puurunen, R.L. Growth per cycle in atomic layer deposition: A theoretical model. *Chem. Vap. Depos.* **2003**, *9*, 249–257. [[CrossRef](#)]
69. Dunn, B.; Long, J.W.; Rolison, D.R. Rethinking multifunction in three dimensions for miniaturizing electrical energy storage. *Electrochem. Soc. Interface* **2008**, *17*, 49–53.
70. Putkonen, M.; Aaltonen, T.; Alnes, M.; Sajavaara, T.; Nilsen, O.; Fjellvåg, H. Atomic layer deposition of lithium containing thin films. *J. Mater. Chem.* **2009**, *19*, 8767–8771. [[CrossRef](#)]
71. Nilsen, O.; Miikkulainen, V.; Gandrud, K.B.; Østreng, E.; Ruud, A.; Fjellvåg, H. Atomic layer deposition of functional films for Li-ion microbatteries. *Phys. Status Solidi A* **2014**, *211*, 357–367. [[CrossRef](#)]
72. Aaltonen, T.; Miikkulainen, V.; Gandrud, K.B.; Pettersen, A.; Nilsen, O.; Fjellvåg, H. ALD of Thin Films for Lithium-Ion Batteries. *ECS Trans.* **2011**, *41*, 331–339. [[CrossRef](#)]
73. Meng, X.; Wang, X.; Geng, D.; Ozgit-Akgun, C.; Schneider, N.; Elam, J.W. Atomic layer deposition for nanomaterial synthesis and functionalization in energy technology. *Mater. Horiz.* **2017**, *4*, 133–154. [[CrossRef](#)]
74. Meng, X.; Elam, J.W. Atomic layer deposition of nanophase materials for electrical energy storage. *ECS Trans.* **2015**, *69*, 39–57. [[CrossRef](#)]
75. Meng, X.; Yang, X.-Q.; Sun, X. Emerging applications of atomic layer deposition for lithium-ion battery studies. *Adv. Mater.* **2012**, *24*, 3589–3615. [[CrossRef](#)] [[PubMed](#)]
76. Guan, C.; Wang, J. Recent development of advanced electrode materials by atomic layer deposition for electrochemical energy storage. *Adv. Sci.* **2016**, *3*, 1500405. [[CrossRef](#)] [[PubMed](#)]
77. Ma, L.; Nuwayhid, R.B.; Wu, T.; Lei, Y.; Amine, K.; Lu, J. Atomic layer deposition for lithium-based batteries. *Adv. Mater. Interfaces* **2016**, *3*, 1600564. [[CrossRef](#)]
78. Nilsen, O.; Gandrud, K.B.; Ruud, A.; Fjellvåg, H. Atomic layer deposition for thin-film lithium-ion batteries. In *Atomic Layer Deposition in Energy Conversion Applications*; Bachmann, J., Ed.; Wiley-VCH Verlag GmbH & Co. KGaA: Weinheim, Germany, 2017; pp. 183–207. ISBN 978-3-527-33912-9.
79. Mäntymäki, M. Atomic Layer Deposition and Lithium-ion Batteries: Studies on New Materials and Reactions for Battery Development. Ph.D. Thesis, University of Helsinki, Helsinki, Finland, 9 June 2017.
80. Liu, J.; Sun, X. Elegant design of electrode and electrode/electrolyte interface in lithium-ion batteries by atomic layer deposition. *Nanotechnology* **2015**, *26*, 024001. [[CrossRef](#)] [[PubMed](#)]
81. Wang, X.; Yushin, G. Chemical vapor deposition and atomic layer deposition for advanced lithium ion batteries and supercapacitors. *Energy Environ. Sci.* **2015**, *8*, 1889–1904. [[CrossRef](#)]
82. Noked, M.; Liu, C.; Hu, J.; Gregorczyk, K.; Rubloff, G.W.; Lee, S.B. Electrochemical thin layers in nanostructures for energy storage. *Acc. Chem. Res.* **2016**, *49*, 2336–2346. [[CrossRef](#)] [[PubMed](#)]
83. Share, K.; Westover, A.; Li, M.; Pint, C.L. Surface engineering of nanomaterials for improved energy storage—A review. *Chem. Eng. Sci.* **2016**, *154*, 3–19. [[CrossRef](#)]
84. Sun, Q.; Lau, K.C.; Geng, D.; Meng, X. Atomic and molecular layer deposition for superior lithium-sulfur batteries: Strategies, performance, and mechanisms. *Batter. Supercaps* **2018**. [[CrossRef](#)]
85. Le Van, K.; Groult, H.; Mantoux, A.; Perrigaud, L.; Lantelme, F.; Lindström, R.; Badour-Hadjean, R.; Zanna, S.; Lincot, D. Amorphous vanadium oxide films synthesised by ALCVD for lithium rechargeable batteries. *J. Power Sources* **2006**, *160*, 592–601. [[CrossRef](#)]
86. Chen, X.; Pomerantseva, E.; Gregorczyk, K.; Ghodssi, R.; Rubloff, G. Cathodic ALD V<sub>2</sub>O<sub>5</sub> thin films for high-rate electrochemical energy storage. *RSC Adv.* **2013**, *3*, 4294–4302. [[CrossRef](#)]
87. Donders, M.E.; Knoops, H.C.M.; Kessels, W.M.M.; Notten, P.H.L. Remote plasma atomic layer deposition of thin films of electrochemically active LiCoO<sub>2</sub>. *ECS Trans.* **2011**, *41*, 321–330. [[CrossRef](#)]

88. Donders, M.E.; Arnoldbik, W.M.; Knoops, H.C.M.; Kessels, W.M.M.; Notten, P.H.L. Atomic layer deposition of LiCoO<sub>2</sub> thin-film electrodes for all-solid-state Li-ion micro-batteries. *J. Electrochem. Soc.* **2013**, *160*, A3066–A3071. [[CrossRef](#)]
89. Liu, J.; Banis, M.N.; Sun, Q.; Lushington, A.; Li, R.; Sham, T.-K.; Sun, X. Rational design of atomic-layer-deposited LiFePO<sub>4</sub> as a high-performance cathode for lithium-ion batteries. *Adv. Mater.* **2014**, *26*, 6472–6477. [[CrossRef](#)] [[PubMed](#)]
90. Miikkulainen, V.; Ruud, A.; Østreng, E.; Nilsen, O.; Laitinen, M.; Sajavaara, T.; Fjellvåg, H. Atomic layer deposition of spinel lithium manganese oxide by film-body-controlled lithium incorporation for thin-film lithium-ion batteries. *J. Phys. Chem. C* **2014**, *118*, 1258–1268. [[CrossRef](#)]
91. Meng, X.; Comstock, D.J.; Fisher, T.T.; Elam, J.W. Vapor-phase atomic-controllable growth of amorphous Li<sub>2</sub>S for high-performance lithium–sulfur batteries. *ACS Nano* **2014**, *8*, 10963–10972. [[CrossRef](#)] [[PubMed](#)]
92. Lantelme, F.; Mantoux, A.; Groult, H.; Lincot, D. Electrochemical study of phase transition processes in lithium insertion in V<sub>2</sub>O<sub>5</sub> electrodes. *J. Electrochem. Soc.* **2003**, *150*, A1202–A1208. [[CrossRef](#)]
93. Gandrud, K.B.; Pettersen, A.; Nilsen, O.; Fjellvåg, H. Growth of LiFePO<sub>4</sub> cathode material by ALD. In Proceedings of the 10th International Conference on Atomic Layer Deposition, Seoul, Korea, 20–23 June 2010.
94. Gandrud, K.B.; Pettersen, A.; Nilsen, O.; Fjellvåg, H. High-performing iron phosphate for enhanced lithium ion solid state batteries as grown by atomic layer deposition. *J. Mater. Chem. A* **2013**, *1*, 9054–9059. [[CrossRef](#)]
95. Kozen, A.C.; Pearce, A.J.; Lin, C.-F.; Schoeder, M.A.; Noked, M.; Lee, S.B.; Rubloff, G.W. Atomic layer deposition and in situ characterization of ultraclean lithium oxide and lithium hydroxide. *J. Phys. Chem. C* **2014**, *118*, 27749–27753. [[CrossRef](#)]
96. Wang, W.; Tian, M.; Abdulagatov, A.; George, S.M.; Lee, Y.-C.; Yang, R. Three-dimensional Ni/TiO<sub>2</sub> nanowire network for high areal capacity lithium ion microbattery applications. *Nano Lett.* **2012**, *12*, 655–660. [[CrossRef](#)] [[PubMed](#)]
97. Cheah, S.K.; Perre, E.; Rooth, M.; Fondell, M.; Hårsta, A.; Nyholm, L.; Boman, M.; Gustafsson, T.; Lu, J.; Simon, P.; et al. Self-supported three-dimensional nanoelectrodes for microbattery applications. *Nano Lett.* **2009**, *9*, 3230–3233. [[CrossRef](#)] [[PubMed](#)]
98. Panda, S.K.; Yoon, Y.; Jung, H.S.; Yoon, W.-S.; Shin, H. Nanoscale size effect of titania (anatase) nanotubes with uniform wall thickness as high performance anode for lithium-ion secondary battery. *J. Power Sources* **2012**, *204*, 162–167. [[CrossRef](#)]
99. Miikkulainen, V.; Nilsen, O.; Laitinen, M.; Sajavaara, T.; Fjellvåg, H. Atomic layer deposition of Li<sub>x</sub>Ti<sub>y</sub>O<sub>z</sub> thin films. *RSC Adv.* **2013**, *3*, 7537–7542. [[CrossRef](#)]
100. Meng, X.; Liu, J.; Li, X.; Banis, M.N.; Yang, J.; Li, R.; Sun, X. Atomic layer deposited Li<sub>4</sub>Ti<sub>5</sub>O<sub>12</sub> on nitrogen-doped carbon nanotubes. *RSC Adv.* **2013**, *3*, 7285–7288. [[CrossRef](#)]
101. Miikkulainen, V.; Nilsen, O.; Laitinen, M.; Sajavaara, T.; Fjellvåg, H. Atomic layer deposition of Li<sub>x</sub>Ti<sub>y</sub>O<sub>z</sub> films. In Proceedings of the 12th International Conference on Atomic Layer Deposition, Dresden, Germany, 17–20 June 2012.
102. Nisula, M.; Karppinen, M. Atomic/molecular layer deposition of lithium terephthalate thin films as high rate capability Li-Ion battery anodes. *Nano Lett.* **2016**, *16*, 1276–1281. [[CrossRef](#)] [[PubMed](#)]
103. Shen, Y.; Søndergaard, M.; Christensen, M.; Birgisson, S.; Iversen, B.B. Solid state formation mechanism of Li<sub>4</sub>Ti<sub>5</sub>O<sub>12</sub> from an anatase TiO<sub>2</sub> source. *Chem. Mater.* **2014**, *26*, 3679–3686. [[CrossRef](#)]
104. Atosuo, E.; Mäntymäki, M.; Mizohata, K.; Heikkilä, M.J.; Räisänen, J.; Ritala, M.; Leskelä, M. Preparation of lithium containing oxides by the solid state reaction of atomic layer deposited thin films. *Chem. Mater.* **2017**, *29*, 998–1005. [[CrossRef](#)]
105. Sundberg, P.; Karppinen, M. Organic and inorganic–organic thin film structures by molecular layer deposition: A review. *Beilstein J. Nanotechnol.* **2014**, *5*, 1104–1136. [[CrossRef](#)] [[PubMed](#)]
106. Armand, M.; Grugeon, S.; Vezin, H.; Laruelle, S.; Ribièrre, P.; Poizot, P.; Tarascon, J.-M. Conjugated dicarboxylate anodes for Li-ion batteries. *Nat. Mater.* **2009**, *8*, 120–125. [[CrossRef](#)] [[PubMed](#)]
107. Nisula, M.; Karppinen, M. In situ lithiated quinone cathode for ALD/MLD-fabricated high-power thin-film battery. *J. Mater. Chem. A* **2018**, *6*, 7027–7033. [[CrossRef](#)]
108. Nisula, M.; Shindo, Y.; Koga, H.; Karppinen, M. Atomic layer deposition of lithium phosphorus oxynitride. *Chem. Mater.* **2015**, *27*, 6987–6993. [[CrossRef](#)]

109. Kozen, A.C.; Pearse, A.J.; Lin, C.-F.; Noked, M.; Rubloff, G.W. Atomic layer deposition of the solid electrolyte LiPON. *Chem. Mater.* **2015**, *27*, 5324–5331. [[CrossRef](#)]
110. Hämäläinen, J.; Munnik, F.; Hatanpää, T.; Holopainen, J.; Ritala, M.; Leskelä, M. Study of amorphous lithium silicate thin films grown by atomic layer deposition. *J. Vac. Sci. Technol. A* **2012**, *30*, 01A106. [[CrossRef](#)]
111. Tomczak, Y.; Knapas, K.; Sundberg, M.; Leskelä, M.; Ritala, M. In situ reaction mechanism studies on lithium hexadimethyldisilazide and ozone atomic layer deposition process for lithium silicate. *J. Phys. Chem. C* **2013**, *117*, 14241–14246. [[CrossRef](#)]
112. Ruud, A.; Miikkulainen, V.; Mizohata, K.; Fjellvåg, H.; Nilsen, O. Enhanced process and composition control for atomic layer deposition with lithium trimethylsilanolate. *J. Vac. Sci. Technol. A* **2017**, *35*, 01B133-1–01B133-8. [[CrossRef](#)]
113. Wang, B.; Liu, J.; Banis, M.N.; Sun, Q.; Zhao, Y.; Li, R.; Sham, T.-K.; Sun, X. Atomic layer deposited lithium silicates as solid-state electrolytes for all-solid-state batteries. *ACS Appl. Mater. Interfaces* **2017**, *9*, 31786–31793. [[CrossRef](#)] [[PubMed](#)]
114. Hämäläinen, J.; Holopainen, J.; Munnik, F.; Hatanpää, T.; Heikkilä, M.; Ritala, M.; Leskelä, M. Lithium phosphate thin films grown by atomic layer deposition. *J. Electrochem. Soc.* **2012**, *159*, A259–A263. [[CrossRef](#)]
115. Wang, B.; Liu, J.; Sun, Q.; Li, R.; Sham, T.-K.; Sun, X. Atomic layer deposition of lithium phosphates as solid-state electrolytes for all-solid-state microbatteries. *Nanotechnology* **2014**, *25*, 504007. [[CrossRef](#)] [[PubMed](#)]
116. Létiche, M.; Eustache, E.; Freixas, J.; Demortière, A.; De Andrade, V.; Morgenroth, L.; Tilmant, P.; Vaurette, F.; Troadec, D.; Roussel, P.; et al. Atomic layer deposition of functional layers for on chip 3D Li-ion all solid state microbattery. *Adv. Energy Mater.* **2017**, *7*, 1601402. [[CrossRef](#)]
117. Liu, J.; Banis, M.N.; Li, X.; Lushington, A.; Cai, M.; Li, R.; Sham, T.-K.; Sun, X. Atomic layer deposition of lithium tantalate solid-state electrolytes. *J. Phys. Chem. C* **2013**, *117*, 20260–20267. [[CrossRef](#)]
118. Østreg, E.; Sønsteby, H.H.; Sajavaara, T.; Nilsen, O.; Fjellvåg, H. Atomic layer deposition of ferroelectric LiNbO<sub>3</sub>. *J. Mater. Chem. C* **2013**, *1*, 4283–4290. [[CrossRef](#)]
119. Wang, B.; Zhao, Y.; Banis, M.N.; Sun, Q.; Adair, K.R.; Li, R.; Sham, T.-K.; Sun, Q. Atomic layer deposition of lithium niobium oxides as potential solid-state electrolytes for lithium-ion batteries. *ACS Appl. Mater. Interfaces* **2018**, *10*, 1654–1661. [[CrossRef](#)] [[PubMed](#)]
120. Aaltonen, T.; Alnes, M.; Nilsen, O.; Costelle, L.; Fjellvåg, H. Lanthanum titanate and lithium lanthanum titanate thin films grown by atomic layer deposition. *J. Mater. Chem.* **2010**, *20*, 2877–2881. [[CrossRef](#)]
121. Perng, Y.-C.; Cho, J.; Sun, S.Y.; Membreno, D.; Cirigliano, N.; Dunn, B.; Chang, J.P. Synthesis of ion conducting Li<sub>x</sub>Al<sub>y</sub>Si<sub>z</sub>O thin films by atomic layer deposition. *J. Mater. Chem. A* **2014**, *2*, 9566–9573. [[CrossRef](#)]
122. Kazyak, E.; Chen, K.-H.; Wood, K.N.; Davis, A.L.; Thompson, T.; Bielinski, A.R.; Sanchez, A.J.; Wang, X.; Wang, C.; Sakamoto, J.; et al. Atomic layer deposition of the solid electrolyte garnet Li<sub>7</sub>La<sub>3</sub>Zr<sub>2</sub>O<sub>12</sub>. *Chem. Mater.* **2017**, *29*, 3785–3792. [[CrossRef](#)]
123. Cao, Y.; Meng, X.; Elam, J.W. Atomic Layer Deposition of Li<sub>x</sub>Al<sub>y</sub>S Solid-state electrolytes for stabilizing lithium-metal anodes. *ChemElectroChem* **2016**, *3*, 858–863. [[CrossRef](#)]
124. Xie, J.; Sendek, A.D.; Cubuk, E.D.; Zhang, X.; Lu, Z.; Gong, Y.; Wu, T.; Shi, F.; Liu, W.; Reed, E.J.; et al. Atomic layer deposition of stable LiAlF<sub>4</sub> lithium ion conductive interfacial layer for stable cathode cycling. *ACS Nano* **2017**, *11*, 7019–7027. [[CrossRef](#)] [[PubMed](#)]
125. Nakagawa, A.; Kuwata, N.; Matsuda, Y.; Kawamura, J. Characterization of stable solid electrolyte lithium silicate for thin film lithium battery. *J. Phys. Soc. Jpn. Suppl. A* **2010**, *79*, 98–101. [[CrossRef](#)]
126. Furusawa, S.; Kamiyama, A.; Tsurui, T. Fabrication and ionic conductivity of amorphous lithium meta-silicate thin film. *Solid State Ion.* **2008**, *179*, 536–542. [[CrossRef](#)]
127. Furusawa, S.; Kasahara, T.; Kamiyama, A. Fabrication and ionic conductivity of Li<sub>2</sub>SiO<sub>3</sub> thin film. *Solid State Ion.* **2009**, *180*, 649–653. [[CrossRef](#)]
128. Liu, J.; Wang, B.; Sun, Q.; Li, R.; Sham, T.-K.; Sun, X. Atomic layer deposition of hierarchical CNTs@FePO<sub>4</sub> architecture as a 3D electrode for lithium-ion and sodium-ion batteries. *Adv. Mater. Interfaces* **2016**, *3*, 1600468. [[CrossRef](#)]
129. Wang, B.; Liu, J.; Sun, Q.; Xiao, B.; Li, R.; Sham, T.-K.; Sun, X. Titanium dioxide/lithium phosphate nanocomposite derived from atomic layer deposition as a high-performance anode for lithium ion batteries. *Adv. Mater. Interfaces* **2016**, *3*, 1600369. [[CrossRef](#)]

130. Shibata, S. Thermal atomic layer deposition of lithium phosphorus oxynitride as a thin-film solid electrolyte. *J. Electrochem. Soc.* **2016**, *163*, A2555–A2562. [[CrossRef](#)]
131. Lin, C.-F.; Noked, M.; Kozen, A.C.; Liu, C.; Zhao, O.; Gregorczyk, K.; Hu, L.; Lee, S.B.; Rubloff, G.W. Solid Electrolyte Lithium Phosphous Oxynitride as a Protective Nanocladding Layer for 3D high-capacity conversion electrodes. *ACS Nano* **2016**, *10*, 2693–2701. [[CrossRef](#)] [[PubMed](#)]
132. Smith, R.T. Elastic, piezoelectric, and dielectric properties of lithium tantalate. *Appl. Phys. Lett.* **1967**, *11*, 146–148. [[CrossRef](#)]
133. Tomeno, I.; Matsumura, S. Dielectric properties of LiTaO<sub>3</sub>. *Phys. Rev. B* **1988**, *38*, 606–614. [[CrossRef](#)]
134. Glass, A.M.; Nassau, K.; Negran, T.J. Ionic conductivity of quenched alkali niobate and tantalate glasses. *J. Appl. Phys.* **1978**, *49*, 4808–4811. [[CrossRef](#)]
135. Li, X.; Liu, J.; Banis, M.N.; Lushington, A.; Li, R.; Cai, M.; Sun, X. Atomic layer deposition of solid-state electrolyte coated cathode materials with superior high-voltage cycling behavior for lithium ion battery application. *Energy Environ. Sci.* **2014**, *7*, 768–778. [[CrossRef](#)]
136. Comstock, D.; Elam, J.W. Mechanistic study of lithium aluminum oxide atomic layer deposition. *J. Phys. Chem. C* **2013**, *117*, 1677–1683. [[CrossRef](#)]
137. Murugan, R.; Thangadurai, V.; Weppner, W. Fast lithium ion conduction in garnet-type Li<sub>7</sub>La<sub>3</sub>Zr<sub>2</sub>O<sub>12</sub>. *Angew. Chem. Int. Ed.* **2007**, *46*, 7778–7781. [[CrossRef](#)] [[PubMed](#)]
138. Meng, X.; Cao, Y.; Libera, J.A.; Elam, J.W. Atomic layer deposition of aluminum sulfide: growth mechanism and electrochemical evaluation in lithium-ion batteries. *Chem. Mater.* **2017**, *29*, 9043–9052. [[CrossRef](#)]
139. Mäntymäki, M.; Mizohata, K.; Heikkilä, M.J.; Räisänen, J.; Ritala, M.; Leskelä, M. Studies on Li<sub>3</sub>AlF<sub>6</sub> thin film deposition utilizing conversion reactions of thin films. *Thin Solid Films* **2017**, *636*, 26–33. [[CrossRef](#)]
140. Nykänen, E.; Soininen, P.; Niinistö, L.; Leskelä, M.; Rauhala, E. Electroluminescent SrS:Ce,F thin films deposited by the atomic layer epitaxy process. In Proceedings of the 1994 International Workshop on Electroluminescence, Beijing, China, 10–12 October 1994; pp. 437–444.
141. Ylilampi, M.; Ranta-aho, T. Metal fluoride thin films prepared by atomic layer deposition. *J. Electrochem. Soc.* **1994**, *141*, 1278–1284. [[CrossRef](#)]
142. Pilvi, T. Atomic Layer Deposition for Optical Applications: Metal fluoride thin films and novel devices. Ph.D. Thesis, University of Helsinki, Helsinki, Finland, 5 December 2008.
143. Lee, Y.; DuMont, J.W.; Cavanagh, A.S.; George, S.M. Atomic Layer Deposition of AlF<sub>3</sub> using trimethylaluminum and hydrogen fluoride. *J. Phys. Chem. C* **2015**, *119*, 14185–14194. [[CrossRef](#)]
144. Park, J.S.; Mane, A.U.; Elam, J.W.; Croy, J.R. Amorphous metal fluoride passivation coatings prepared by atomic layer deposition on LiCoO<sub>2</sub> for Li-ion batteries. *Chem. Mater.* **2015**, *27*, 1917–1920. [[CrossRef](#)]
145. Jackson, D.H.K.; Laskar, M.R.; Fang, S.; Xu, S.; Ellis, R.G.; Li, X.; Dreibelbis, M.; Babcock, S.E.; Mahanthappa, M.K.; Morgan, D.; et al. Optimizing AlF<sub>3</sub> atomic layer deposition using trimethylaluminum and TaF<sub>5</sub>: Application to high voltage Li-ion battery cathodes. *J. Vac. Sci. Technol. A* **2016**, *34*, 031503-1–031503-8. [[CrossRef](#)]
146. Lee, Y. Atomic layer etching of metal oxides and atomic layer deposition of metal fluorides. Ph.D. Thesis, University of Colorado, Boulder, CO, USA, January 2015.
147. Lee, Y.; Sun, H.; Young, M.J.; George, S.M. Atomic layer deposition of metal fluorides using HF–pyridine as the fluorine precursor. *Chem. Mater.* **2016**, *28*, 2022–2032. [[CrossRef](#)]
148. Hennessy, J.; Jewell, A.P.; Greer, F.; Lee, M.C.; Nikzad, S. Atomic layer deposition of magnesium fluoride via bis(ethylcyclopentadienyl)magnesium and anhydrous hydrogen fluoride. *J. Vac. Sci. Technol. A* **2015**, *33*, 01A125. [[CrossRef](#)]
149. Hennessy, J.; Jewell, A.D.; Balasubramanian, K.; Nikzad, S. Ultraviolet optical properties of aluminum fluoride thin films deposited by atomic layer deposition. *J. Vac. Sci. Technol. A* **2016**, *34*, 01A120. [[CrossRef](#)]
150. Mäntymäki, M.; Hämäläinen, J.; Puukilainen, E.; Munnik, F.; Ritala, M.; Leskelä, M. Atomic layer deposition of LiF thin films from lithd and TiF<sub>4</sub> precursors. *Chem. Vap. Depos.* **2013**, *19*, 111–116. [[CrossRef](#)]
151. Mäntymäki, M.; Hämäläinen, J.; Puukilainen, E.; Sajavaara, T.; Ritala, M.; Leskelä, M. Atomic layer deposition of LiF thin films from Lithd, Mg(thd)<sub>2</sub>, and TiF<sub>4</sub> precursors. *Chem. Mater.* **2013**, *25*, 1656–1663. [[CrossRef](#)]
152. Mane, A.; Libera, J.; Elam, J. Atomic layer deposition of LiF thin films using lithium tert-butoxide and metal fluoride precursors. In Proceedings of the 16th International Conference on Atomic Layer Deposition, Dublin, Ireland, 24–27 July 2016.

153. Pilvi, T.; Hatanpää, T.; Puukilainen, E.; Arstila, K.; Bischoff, M.; Kaiser, U.; Kaiser, N.; Leskelä, M.; Ritala, M. Study of a novel ALD process for depositing  $\text{MgF}_2$  thin films. *J. Mater. Chem.* **2007**, *17*, 5077–5083. [[CrossRef](#)]
154. Pilvi, T.; Puukilainen, E.; Kreissig, U.; Leskelä, M.; Ritala, M. Atomic layer deposition of  $\text{MgF}_2$  thin films using  $\text{TaF}_5$  as a novel fluorine source. *Chem. Mater.* **2008**, *20*, 5023–5028. [[CrossRef](#)]
155. Pilvi, T.; Arstila, K.; Leskelä, M.; Ritala, M. Novel ALD process for depositing  $\text{CaF}_2$  thin films. *Chem. Mater.* **2007**, *19*, 3387–3392. [[CrossRef](#)]
156. Mäntymäki, M.; Heikkilä, M.J.; Puukilainen, E.; Mizohata, K.; Marchand, B.; Räisänen, J.; Ritala, M.; Leskelä, M. Atomic layer deposition of  $\text{AlF}_3$  thin films using halide precursors. *Chem. Mater.* **2015**, *27*, 604–611. [[CrossRef](#)]
157. Pilvi, T.; Puukilainen, E.; Munnik, F.; Leskelä, M.; Ritala, M. ALD of  $\text{YF}_3$  thin films from  $\text{TiF}_4$  and  $\text{Y}(\text{thd})_3$  precursors. *Chem. Vap. Depos.* **2009**, *15*, 27–32. [[CrossRef](#)]
158. Pilvi, T.; Puukilainen, E.; Arstila, K.; Leskelä, M.; Ritala, M. Atomic layer deposition of  $\text{LaF}_3$  thin films using  $\text{La}(\text{thd})_3$  and  $\text{TiF}_4$  as precursors. *Chem. Vap. Depos.* **2008**, *14*, 85–91. [[CrossRef](#)]
159. Park, J.S.; Mane, A.U.; Elam, J.W.; Croy, J.R. Atomic layer deposition of Al–W–Fluoride on  $\text{LiCoO}_2$  cathodes: Comparison of particle- and electrode-level coatings. *ACS Omega* **2017**, *2*, 3724–3729. [[CrossRef](#)]
160. Putkonen, M.; Szeghalmi, A.; Pippel, E.; Knez, M. Atomic layer deposition of metal fluorides through oxide chemistry. *J. Mater. Chem.* **2011**, *21*, 14461–14465. [[CrossRef](#)]
161. Vos, M.F.J.; Knoops, H.C.M.; Synowicki, R.A.; Kessels, W.M.M.; Mackus, A.J.M. Atomic layer deposition of aluminum fluoride using  $\text{Al}(\text{CH}_3)_3$  and  $\text{SF}_6$  plasma. *Appl. Phys. Lett.* **2017**, *111*, 113105-1–113105-5. [[CrossRef](#)]
162. Bridou, F.; Cuniot-Ponsard, M.; Desvignes, J.-M.; Richter, M.; Kroth, U.; Gottwald, A. Experimental determination of optical constants of  $\text{MgF}_2$  and  $\text{AlF}_3$  thin films in the vacuum ultra-violet wavelength region (60–124 nm), and its application to optical designs. *Opt. Commun.* **2010**, *283*, 1351–1358. [[CrossRef](#)]
163. Sun, J.; Li, X.; Zhang, W.; Yi, K.; Shao, J. Effects of substrate temperatures and deposition rates on properties of aluminum fluoride thin films in deep-ultraviolet region. *Appl. Opt.* **2012**, *51*, 8481–8489. [[CrossRef](#)] [[PubMed](#)]
164. König, D.; Scholz, R.; Zahn, D.R.T.; Ebest, G. Band diagram of the  $\text{AlF}_3/\text{SiO}_2/\text{Si}$  system. *J. Appl. Phys.* **2005**, *97*, 093707-1–093707-9. [[CrossRef](#)]
165. Song, G.-M.; Wu, Y.; Liu, G.; Xu, Q. Influence of  $\text{AlF}_3$  coating on the electrochemical properties of  $\text{LiFePO}_4$ /graphite Li-ion batteries. *J. Alloy. Compd.* **2009**, *487*, 214–217. [[CrossRef](#)]
166. Lee, D.-J.; Lee, K.-S.; Myung, S.-T.; Yashiro, H.; Sun, Y.-K. Improvement of electrochemical properties of  $\text{Li}_{1.1}\text{Al}_{0.05}\text{Mn}_{1.85}\text{O}_4$  achieved by an  $\text{AlF}_3$  coating. *J. Power Sources* **2011**, *196*, 1353–1357. [[CrossRef](#)]
167. Lee, H.J.; Kim, S.B.; Park, Y.J. Enhanced electrochemical properties of fluoride-coated  $\text{LiCoO}_2$  thin films. *Nanoscale Res. Lett.* **2012**, *7*, 16. [[CrossRef](#)] [[PubMed](#)]
168. Lapiano-Smith, D.A.; Eklund, E.A.; Himpfel, F.J.; Terminello, L.J. Epitaxy of LiF on Ge(100). *Appl. Phys. Lett.* **1991**, *59*, 2174–2176. [[CrossRef](#)]
169. Li, H.H. Refractive index of alkali halides and its wavelength and temperature derivatives. *J. Phys. Chem. Ref. Data* **1976**, *5*, 329–528. [[CrossRef](#)]
170. Lee, Y.; Huffman, C.; George, S.M. Selectivity in thermal atomic layer etching using sequential, self-limiting fluorination and ligand-exchange reactions. *Chem. Mater.* **2016**, *28*, 7657–7665. [[CrossRef](#)]
171. Zywootko, D.R.; George, S.M. Thermal atomic layer etching of ZnO by a “Conversion-Etch” mechanism using sequential exposures of hydrogen fluoride and trimethylaluminum. *Chem. Mater.* **2017**, *29*, 1183–1191. [[CrossRef](#)]
172. DuMont, J.W.; George, S.M. Competition between  $\text{Al}_2\text{O}_3$  atomic layer etching and  $\text{AlF}_3$  atomic layer deposition using sequential exposures of trimethylaluminum and hydrogen fluoride. *J. Chem. Phys.* **2017**, *146*, 052819. [[CrossRef](#)] [[PubMed](#)]
173. Zhou, Y.; Lee, Y.; Sun, H.; Wallas, J.M.; George, S.M.; Xie, M. Coating solution for high-voltage cathode:  $\text{AlF}_3$  atomic layer deposition for freestanding  $\text{LiCoO}_2$  electrodes with high energy density and excellent flexibility. *ACS Appl. Mater. Interfaces* **2017**, *9*, 9614–9619. [[CrossRef](#)] [[PubMed](#)]
174. Rousseau, F.; Jain, A.; Kostas, T.T.; Hampden-Smith, M.; Farr, J.D.; Muenchausen, R. Low-temperature dry etching of metal oxides and ZnS via formation of volatile metal  $\beta$ -diketonate complexes. *J. Mater. Chem.* **1992**, *2*, 893–894. [[CrossRef](#)]

175. Ritala, M.; Leskelä, M.; Nykänen, E.; Soininen, P.; Niinistö, L. Growth of titanium dioxide thin films by atomic layer epitaxy. *Thin Solid Films* **1993**, *225*, 288–295. [[CrossRef](#)]
176. Miikkulainen, V.; Leskelä, M.; Ritala, M.; Puurunen, R.L. Crystallinity of inorganic films grown by atomic layer deposition: Overview and general trends. *J. Appl. Phys.* **2013**, *113*, 021301-1–021301-101. [[CrossRef](#)]
177. Krause, R.F., Jr.; Douglas, T.B. Heats of formation of  $\text{AlClF}_2$  and  $\text{AlCl}_2\text{F}$  from subliming aluminum fluoride in the presence of aluminum chloride vapor. *J. Phys. Chem.* **1968**, *72*, 3444–3451. [[CrossRef](#)]
178. Haukka, S. ALD technology—Present and future challenges. *ECS Trans.* **2007**, *3*, 15–26. [[CrossRef](#)]
179. Klug, J.A.; Proslie, T.; Elam, J.W.; Cook, R.E.; Hiller, J.M.; Claus, H.; Becker, N.G.; Pellin, M.J. Atomic layer deposition of amorphous niobium carbide-based thin film superconductors. *J. Phys. Chem. C* **2011**, *115*, 25063–25071. [[CrossRef](#)]
180. Kaipio, M.; Kemell, M.; Vehkamäki, M.; Mattinen, M.; Mizohata, K.; Ritala, M.; Leskelä, M. Atomic layer deposition of metal carbides—The  $\text{TiCl}_4$ /TMA process as an example. In Proceedings of the 14th Baltic Conference on Atomic Layer Deposition, St. Petersburg, Russia, 2–4 October 2016.
181. Chen, Y.; Ould-Chikh, S.; Abou-Hamad, E.; Callens, E.; Mohandas, J.C.; Khalid, S.; Basset, J.-M. Facile and efficient synthesis of the surface tantalum hydride  $(\equiv\text{SiO})_2\text{Ta}^{\text{III}}\text{H}$  and tris-siloxy tantalum  $(\equiv\text{SiO})_3\text{Ta}^{\text{III}}$  starting from novel tantalum surface species  $(\equiv\text{SiO})\text{TaMe}_4$  and  $(\equiv\text{SiO})_2\text{TaMe}_3$ . *Organometallics* **2014**, *33*, 1205–1211. [[CrossRef](#)]
182. Schrock, R.R.; Meakin, P. Pentamethyl complexes of niobium and tantalum. *J. Am. Chem. Soc.* **1974**, *96*, 5288–5290. [[CrossRef](#)]
183. Nilsen, O.; Fjellvåg, H.; Kjekshus, A. Growth of calcium carbonate by the atomic layer chemical vapour deposition technique. *Thin Solid Films* **2004**, *450*, 240–247. [[CrossRef](#)]



© 2018 by the authors. Licensee MDPI, Basel, Switzerland. This article is an open access article distributed under the terms and conditions of the Creative Commons Attribution (CC BY) license (<http://creativecommons.org/licenses/by/4.0/>).